CZECH TECHNICAL UNIVERSITY IN PRAGUE

Radiation Effects In Semiconductor Detectors

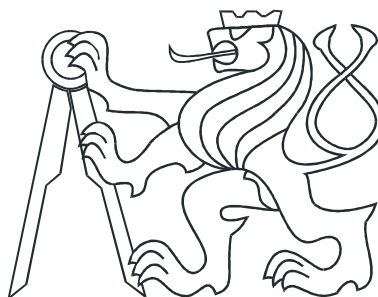*Author:*
Bc. Markéta SEDLÁČKOVÁ

Supervisor:
Prom. fyz. Václav VRBA, CSc.

Faculty of Nuclear Sciences and Physical Engineering

Department of Physics

Prague, 2014

Prohlášení:

Prohlašuji, že jsem svou diplomovou práci vypracoval samostatně a použil jsem pouze podklady (literaturu, software, atd.) uvedené v přiloženém seznamu.

Nemám závažný důvod proti užití tohoto školního díla ve smyslu Zákona 60.121/2000 Sb., o právu autorském, o právech souvisejících s právem autorským a o změně některých zákonů (autorský zákon).

V Praze dne: ....

Podpis

Title:
Radiation effects in semiconductor detectors

Author: Markéta Sedláčková

Specialization: Experimental nuclear and particle physics

Sort of project: Diploma thesis

Supervisor: Prom. fyz. Václav Vrba, CSc.

Abstract: In this thesis the radiation effects in semiconductor detectors, both in the sensor and the electronics, were studied. A measurement of radiation effects and their analysis was performed. The measurement took place at the light water nuclear reactor LVR-15 of the Research Centre Rez Ltd. For the studied measurement, semiconductor circuits were irradiated by combined neutron and gamma fields. Test structures consisting of MOSFET transistors were analyzed. It was shown that their current-voltage characteristics change with irradiation. Also, the threshold voltage of these test structures was discussed as well as the radiation induced shift of its value. Mobility degradation was observed as a result of the vertical field mobility degradation effect and the radiation damage induced to the chip. Current consumption of the chips after irradiation by neutron fluence of $3 \cdot 10^{15}$ n/cm^{-2} for 60 s has in average raised for both the analog and digital current by 10 %.

Key words: Radiation effects, Ionization, MOS, neutron

Název práce:
Radiační efekty v polovodičových detektorech záření

Autor: Markéta Sedláčková

Vedoucí: Prom. fyz. Václav Vrba, CSc.

Abstrakt: Tato diplomová práce se zabývá studiem radiačních efektů v polovodičových detektorech záření a jeho částech: v senzorech i elektronice. Bylo provedeno měření vlastností testovacích vzorků před a po ozáření, které se uskutečnilo na jaderném reaktoru LVR-15 v Řeži ve směsném poli neutronů a fotonů. Měřené struktury byly tranzistory, které byly součástí integrovaného obvodu. Byly zkoumány voltampérové charakteristiky MOSFET tranzistorů a byla pozorována jejich změna po ozáření. Dále byl studován posuv prahového napětí a diskutován vliv radiačního poškození na jeho chování. Bylo pozorováno snížení mobility vlivem dvou efektů: příčného působení elektrického pole a vlivem radiačního poškození čipu. Analogová i digitální spotřeba proudu čipů po ozáření dávkou neutronů $3 \cdot 10^{15}$ n/cm^{-2} za 60 s vzrostla v průměru o 10 %.

Klíčová slova: Radiační efekty, Ionizace, MOS, neutron

Acknowledgements:

Contents

Introduction

The first chapter of this thesis is intended as an introduction to the subatomic world and its interactions. The elementary building blocks of the matter are introduced. The second part of the chapter deals with interactions of particles with matter and possible laboratory-scale sources of these particles. The third and last part of this chapter presents variables used to measure the fluence of and damage caused by the particles described before.

The second chapter is dedicated to semiconductors; their properties and applications. This chapter is focused on silicon and its uses, as it is currently the most commonly used semiconducting element. Next, the possible dopations, p-n junction, MOS structure and transistor devices are described. At this point, the chapter starts to describe the silicon particle detectors with focus on position sensitive detectors. The production of detector-grade silicon is described as it is later its further processing. The chapter concludes with a description of a currently used silicon pixel detector located at the ATLAS experiment at CERN.

The third chapter is focused on radiation damage to silicon radiation detectors and readout electronics. Radiation hard materials are those that withstand radiation damage with minor changes in their operating properties. This chapter describes which various damage mechanisms can take place in irradiated detectors and later describes the evolution of these effects in time.

The fourth and last chapter is dedicated to the analysis of radiation effects of irradiated silicon structures. Set of measurements of the chip properties were performed before and after irradiation. The measurement took place in April 2014 at the nuclear research reactor of the research organisation Research Centre Rez Ltd. The electrical structures studied in this thesis are arrays of MOSFET transistors of various types and dimensions. The results are presented including current-voltage characteristics, threshold voltage and mobility degradation of the studied test structures. Current consumption of the measured chips is also discussed.

Interactions of particles

This chapter is dedicated to the brief description of basic concepts of the interaction of elementary particles of which the Standard model constitues. In this chapter are described also processes which take place in passage of particles through matter.

The first section of this chapter is thus dedicated to the basic theoretical frame – the Standard model of fundamental particles and interactions. In the second part of the chapter, different types of interactions of particles with matter will be presented. This section is based on the classification made by Knoll [1]. The third part of this chapter is dedicated to the introduction to dosimetry, study of quantification of the radiation dose caused by the ionizing radiation.

1.1 The Standard Model

The Standard model of fundamental particles and interactions describes the basic building blocks of the observable universe[1]. The dimensions of these elementary particles are less than 10^{-18} m and they are assumed to be point-like entities. The interactions between particles are mediated by the gauge bosons in the framework of the Standard model.

This theoretical and experimental framework consists of twelve elementary matter particles and their antimatter counterparts, twelve mediating particles and the Higgs boson. Basic properties of matter and mediating particles are listed in Table 1.1 and 1.2 respectively[2]; in both tables, the experimental and statistical uncertainties are not shown. The twelve various matter particles are 6 quarks and 6 leptons, whereas the twelve intermediating particles are 8 gluons, 2 charged W bosons, a neutral Z boson and a photon.

1.1.1 Fundamental interactions

There are four fundamental interactions that describe how all particles interact with each other. Each of them will now be shortly introduced.

Gravitation

The weakest of all, gravity is an interaction that attracts objects with a force proportional to their mass. It is the force behind planets keeping their orbits around Sun or, for example, Moon around Earth. However, on the particle physics scale, its effects become negligible compared to

---

[1]In fact, their contribution to the mass-energy of the known universe is only 4.9%. The rest is constituted of dark matter (26.8%) and dark energy (68.3%), which will not be discussed in this thesis. [2]

[2]Electronvolt (eV) is a unit used in particle physics defined as 1 eV = 1.602×10^{-19} J.

	QUARKS					LEPTONS			
	Name	Q	Mass [MeV]			Name	Q	Mass [MeV]
u	Up	$+2/3$	1.7 to 3.3		ν_e	e^- neutrino	0	< 0.0000022
d	Down	$-1/3$	4.1 to 5.8		e^-	Electron	-1	0.51
c	Charm	$+2/3$	1180 to 1340		ν_μ	μ^- neutrino	0	< 0.17
s	Strange	$-1/3$	80 to 130		μ^-	Muon	-1	105.66
t	Top	$+2/3$	$(156 \text{ to } 165) \times 10^3$		ν_τ	τ^- neutrino	0	< 15.5
b	Bottom	$-1/3$	4130 to 4350		τ^-	Tau	-1	1776.84

Table 1.1: Fundamental particles and their properties. Spin $S = 1/2$ for all these particles and Q denotes their charge. Values from [3].

	Name	Q	S	Mass [GeV]
g	Gluon	0	1	0
γ	Photon	0	1	0
Z^0	Z boson	0	1	91.2
$W^\pm$	W boson	± 1	1	80.4
H	Higgs boson	0	0	126

Table 1.2: Interaction mediators and their basic properties. Q denotes electric charge. Values from [3].

other forces, which then leads to an actual omitting of gravity from elementary particle physics. A physical theory describing gravity is the (classical) Newton's law of gravity and Einstein's general theory of relativity. A widely accepted quantum theory of gravity has yet to be found. Graviton is a hypothetical particle of no mass and no electric charge with spin 2 that mediates the gravitational force.

Electromagnetic interaction

This interaction acts between electrically charged particles and can be completely described by Maxwells' equations [4]. It causes atoms and molecules to hold together by binding the positively charged nuclei to the negatively charged electrons. Moreover, it is responsible for light and other electromagnetic radiation; magnetism and electricity are both caused by this interaction. Quantum electromagnetic theory is called quantum electrodynamics (QED), comes in 1940s and employs the photon as a mediating particle (vector boson).

Weak interaction

Weak force inherited its name from the fact that it seems weak compared to the strong or electromagnetic interaction. It is the only interaction in the framework of the Standard model capable of changing one type of quark into another (i.e., changing their flavour). Most common example is the beta decay of a neutron, in which one *down* quark changes to an *up* quark. It is also responsible for the decay of muons. It violates parity and even CP symmetry. The carriers of this interaction are $W^\pm$ and Z^0 bosons, very heavy particles that are causing the relative slowness and short range of this interaction.

A theory, which unifies the weak and electromagnetic interaction between elementary particles, is called the electroweak theory. It is also known as the Glashow-Weinberg-Salam (GWS) theory.

These two interactions seem different at low energies, but above the unification energy (of the order of 100 GeV) they merge into one. The electroweak theory was suggested in 1960s and it has been experimentally verified in 1973 (discovery of the neutral currents) and 1982 (discovery of the W and Z bosons). It incorporates the Higgs mechanism in order to generate masses for the heavy vector bosons and predicts the existence of the scalar Higgs boson via spontaneous symmetry breaking (for more information on the subject and proper derivation, see Ref. [5]).

Strong interaction

Strong force does not only bind quarks into hadrons, but higher momenta of the strong force also hold together nucleons in nuclei. The theory of the strong force is called quantum chromodynamics (QCD), it emerged in the 1960s, and uses massless gluons as mediators and is nowadays the most precise theory to describe strong interaction. This theory introduces new quantum number called color. According to the model, particles that interact under strong interaction carry a color charge (denoted red, green, blue).

1.1.2 Fundamental particles

Elementary matter particles are called quarks and leptons. There are six quarks in three generations: up and down, charm and strange, top and bottom. Different types of quarks are usually denoted as flavours. As already mentioned above, to each quark there is an antiquark, which has the same properties as its respective quark, but the electric charge has an opposite sign. The uncertainties of the masses of quarks written in Table 1.1 are caused by the fact that quarks have not been observed freely floating around. The only exception to this rule is the top quark, whose mean lifetime is so short, that it decays before hadronization[3] can take place.

Shortly after creation quarks form bound states called mesons and baryons. Baryons are bound states of three quarks qqq (or three antiquarks $\bar{q}\bar{q}\bar{q}$). All baryons except proton (uud) are unstable. Other examples of baryons are neutron (udd), Ω^{--} (sss) or Λ^0 (uds). Mesons are bound states of quark q and antiquark $\bar{q}$ and are all unstable. Examples of mesons are J/ψ (c$\bar{\text{c}}$), kaons K$^{+/0/-}$ (u$\bar{\text{s}}$/d$\bar{\text{s}}$ or s$\bar{\text{d}}$/s$\bar{\text{u}}$) or pions $\pi^{+/0/-}$ (u$\bar{\text{d}}$/u$\bar{\text{u}}$ or d$\bar{\text{d}}$/d$\bar{\text{u}}$). The discovery of quark structure of nucleons happened in 1968, when deep inelastic scattering experiments at the Stanford Linear Accelerator Center (SLAC) showed the existence of an inner structure of nucleons.

The remaining six elementary fermion particles are leptons. They are again arranged in three generations: electronic, muonic and tauonic leptons and to each lepton there exists a neutrino. The naming for antileptons comes with one exception to the standard rule of adding an *anti-* prefix to the lepton's name – due to historical reasons, antielectron was given the name positron.

1.1.3 Composite systems

The above introduced elementary particles of the first generation (u and d quark, electron) form the observable universe. Protons and neutrons form a nucleus that holds together through a residual strong interaction. This positively charged centre is surrounded with negatively charged electrons forming an atom. The nucleus is bound to electrons via the electromagnetic force. The dimensions are as follows: quarks are assumed to be point-like (or smaller than 10^{-18} m).A proton/neutron is of the size $\approx 10^{-15}$ m, a nucleus is $\approx 10^{-14}$ m, electrons are again point-like and smaller than 10^{-18} m, and finally dimensions of an atom are of the order of 10^{-10} m.

The standard labeling of atomic isotopes is represented as follows:

$$^A_Z\text{X}, \tag{1.1}$$

---

[3]Hadronization is defined as a process of the formation of hadrons out of quarks and gluons.

where X is the studied nuclear species with A denoting its mass (nucleon) number and Z its atomic (proton) number. Proton number Z is defined as the number of protons in the nucleus and subsequently the number of adjoint electrons. Nucleon number A is defined as the number of nucleons in atoms, i.e. $A = Z + N$, where N is the number of neutrons in the nucleus. It should be noted, that the measured mass of the isotope is not equal to the mass number A in the appropriate units, but varies slightly due to the binding energy.

1.2   Passage of particles through matter

Particles passing through matter are detected via the mechanisms with which they interact and lose energy in matter. The classification used in this thesis is based on the Ref. [1]. It is convenient to divide all interacting particles into following groups according to their nature and different mechanisms through which they manifest themself:

- ◆ Charged particles
- ◆ Electrons

- ◆ Neutrons
- ◆ X-rays and gamma rays

Particles in the first column are *charged*, which makes their identification easier – they constantly interact with the surrounding environment through the electromagnetic force. Charged particles are divided into two groups: the so called heavy charged particles and electrons. Eventhough both types are charged, due to their different interaction mechanisms they are classified into two groups. The difference, as the name suggests, lays in their mass – electrons are 100 times lighter than the lightest of the heavy charged. Also, electrons were put into special category, because they manifest themselves via bremsstrahlung, a process of importance only to light particles. The second column consists of *uncharged* particles that do not automatically interact with matter. If they are made to interact in the environment, they can be identified through secondary charged particles.

1.2.1   Heavy charged particles

Heavy charged particles are particles with either their mass number greater than one, such as alpha particle, proton, deuteron, fission fragments, or particles of high energy such as muons, pions or kaons.

The laboratory-scale sources of these particles are alpha decay, spontaneous fission or the outcomes of high energy physics experiments. Alpha decay can be schematically written as

$$^{A}_{Z}\text{X} \rightarrow\ ^{A-4}_{Z-2}\text{Y} +\ ^{4}_{2}\alpha,$$
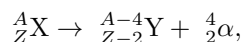
where X and Y are the initial and final nuclear species with A and Z defined in 1.1. The energy of alpha particles resulting from this decay is mostly between 4 and 6 MeV.

Fission is a process that happens to heavy nuclei that yields energetic heavy particles called fission fragments. This process cannot be schematically written because the fission fragments differ for each nucleus; also a number of fast neutrons and gamma rays is released. Because of the nature of a multiple-body decay, the mass numbers of the fission fragments are not defined precisely, but follow a statistical distribution similar to the one of ^{252}Cf shown in Fig. 1.1.

In theory, spontaneous fission can happen to all particles heavier than alpha particle, but, because of the size of the potential barrier, it happens only to isotopes with large mass number. The criterion for whether spontaneous fission can occur in a time short enough to be observed by present methods is:
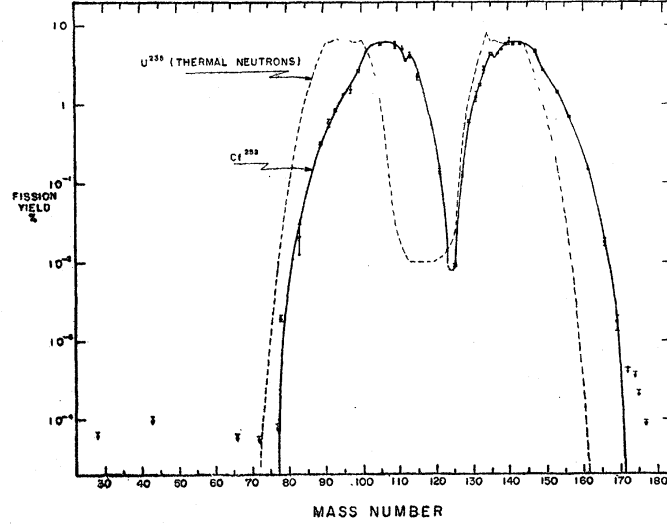
$$\frac{Z^2}{A} \geq 47,$$

Figure 1.1: The mass distribution of ^{252}Cf spontaneous fission fragments. The corresponding distribution from fission of ^{235}U induced by thermal neutrons is also shown. [6]

where A and Z are defined in 1.1. This formula is derived from the liquid drop model.

Heavy charged particles interact with their surroundings and lose their energy through four different processes:

◆ Excitation and ionization of atoms   ◆ Electron capture

◆ Elastic scattering   ◆ Polarization of atoms (high energy process)

These processes are based on the interaction of positively charged heavy particles with negatively charged electrons of the medium atoms; heavy charged particles interact mainly with electrons of the absorber atom and only rarely with the atom nuclei. Excitation of the absorber atom happens when a passing particle raises an electron to a higher-energy shell, while ionization of the atom is when the electron is completely removed from the atom. This free electron may either recombine with the ion of the absorber atom, or, if it is of enough kinetic energy, it may further ionize its surroundings. Such an energetic electron is called delta electron. The process, in which the absorber atom is left ionized but no electron is freed, is called electron capture. In this process the nucleus absorbs an inner electron, thus ionizing itself.

The particle eventually stops or decays in the medium. The *linear stopping power S* for charged particles is defined as:

$$S = -\frac{dE}{dx},$$

where the value of $-dE/dx$ along a particle track is also called the *specific energy loss*. The classical expression used to describe specific energy loss is called the Bethe formula, and is written as:

$$-\left\langle \frac{dE}{dx} \right\rangle = \left(\frac{e^2}{4\pi\epsilon_0} \right)^2 \frac{4\pi Z^2 n_e}{m_e c^2 \beta^2} \left[\frac{1}{2} \ln \frac{2m_e c^2 \beta^2 \gamma^2 T_{\max}}{I^2} - \beta^2 - \frac{\delta(\beta\gamma)}{2} \right], \qquad (1.2)$$

where v and Ze are the velocity and charge of the primary particle, n_e is the electron density of the absorber, m_e is the electron rest mass, e is the electronic charge, ϵ_0 is the vacuum permitivity,
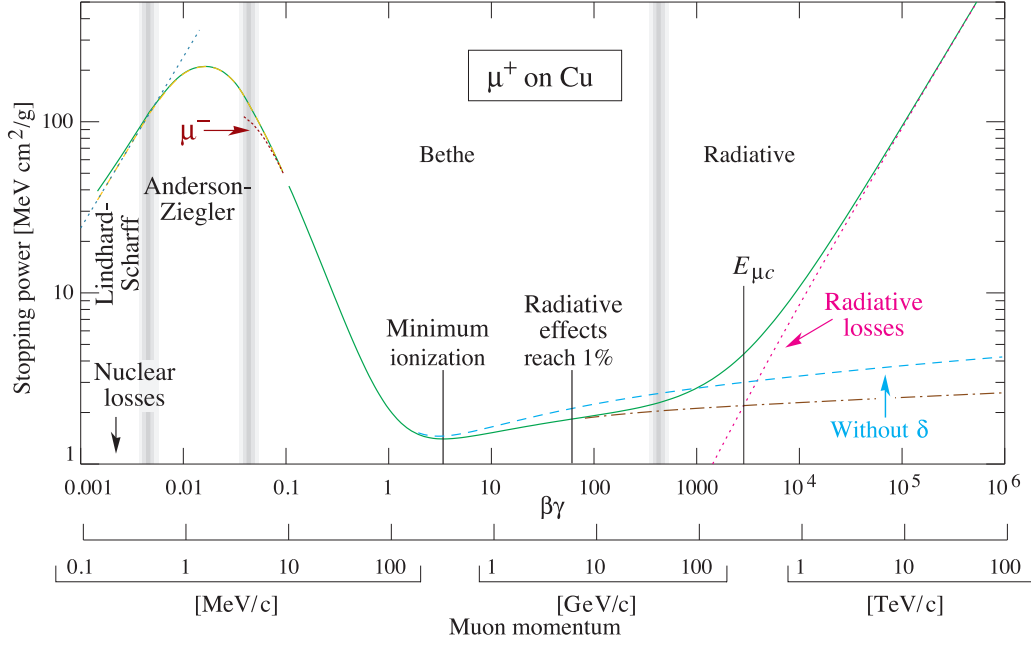
Figure 1.2: Stopping power $(= -\langle dE/dx \rangle)$ for positive muons in copper as a function of $\beta\gamma = p/Mc$ over nine orders of magnitude in momentum (12 orders of magnitude in kinetic energy). [3]

I is the mean excitation potential of the target, $T_{\max}$ is the maximum kinetic energy which can be imparted to a free electron in a single collision and $\delta(\beta\gamma)$ is the density effect correction to ionization energy loss. β is used to denote a fraction v/c, where c is the speed of light in vacuum [3].

The electron density n_e is defined as:

$$n_e = \frac{N_A z \rho}{a M_\mu},$$

where N_A is the Avogadro constant, a and z are the mass and atomic number of the absorber, ρ is its density and M_μ is the molar mass constant. The experimental formula for the mean excitation potential is $I = 13.5 \cdot Z$, where Z is the atomic number of the absorber. The maximum imparted kinetic energy $T_{\max}$ is defined as:

$$T_{\max} = \frac{2 m_e c^2 \beta^2 \gamma^2}{1 + 2\gamma m_2/M + (m + M)^2},$$

where M is the particle mass and $M\beta\gamma c$ is its momentum.

In Fig. 1.2, the stopping power of a positive muon in copper is plotted. Solid line indicates the total stopping power. It is convenient to divide the curve into several sections that display different properties. In the momentum range up to 1 MeV/c, the Bethe formula is not valid, because the charge exchange between the particle and the absorber, which is not described by this formula, becomes important. In the following energy region (1 MeV/c to 1 GeV/c), the Bethe formula 1.2 can be approximated as: $-dE/dx \approx 1/v^2 \approx 1/E$; the ionization loss increases as the particle velocity decreases. At the end of this section there is an interval of minimum ionization. Particles within this energetic range are often called MIPs = Minimum Ionizing Particles and because of the
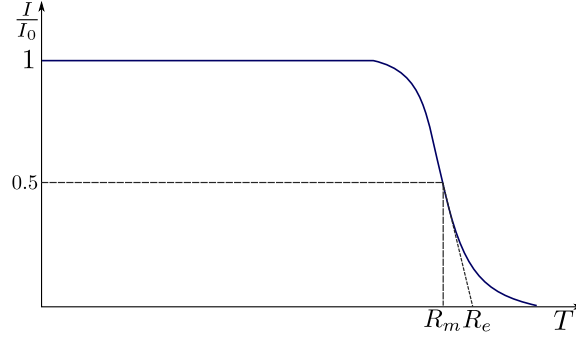
7

Figure 1.3: Intensity of alpha particle beam.

minimal ionization their energy is harder to determine purely by ionization alone; examples of these particles are energetic muons. Before the radiative effects start taking place (in the range above several GeV/c), the Bethe formula can be approximated as: $-dE/dx \approx \ln E$.

Particle range

Because of the nature of heavy charged particles, their range can be defined. The particle passes through the medium in a straight line and the distance which the particle passes in the absorber is called range. This is due to the fact that the particle loses only a small fraction of energy per interaction during its passage through the absorber and interactions occur in all directions at the same time, resulting into an undeflected passage of the particle through the absorber.

Fig. 1.3 shows a dependence of the relative intensity of alpha particle beam I/I_0 on the absorber thickness T. It is clear that alpha particles pass some range without diminuation, and then their intensity suddenly drops to zero. The mean range R_m is defined as the absorber thickness which reduces the alpha particle intensity to one half; extrapolated range R_e is obtained by an extrapolation of the linear portion of the end of the transmission curve to zero.

Landau distribution

Energy loss follows a statistical distribution represented by a Landau distribution. This means that when a particle of a given energy enters the detector, the energy deposited (and read out) fluctuates around the average value given by the Bethe formula (see Eq. 1.2). The outcome of the statistical fluctuations can be seen in Fig. 1.4.

The probability density for value x in the Landau distribution is proportional to :

$$P(x) = \int_0^\infty \sin(2t) \exp - \left(\frac{(x-\mu)t}{\sigma} + \frac{2}{\pi} t \log t \right) dt, \tag{1.3}$$

where μ is the location parameter, σ is the scale parameter and t is the variable of integration. In Fig. 1.4, the probability density is shifted by $\mu = 2$ and is scaled by $\sigma = 1$ [7].

Bragg curve

The Bragg curve, which is shown in Fig. 1.5, describes the stopping power as a function of charged particle path in the material. As can be seen from the figure, the stopping power increases as $1/E$ until it quickly drops to zero. This phenomenon is called the Bragg peak and is of importance in radiation therapy, where it is used to concentrate the energy deposit effect of ions on the treated tumor.
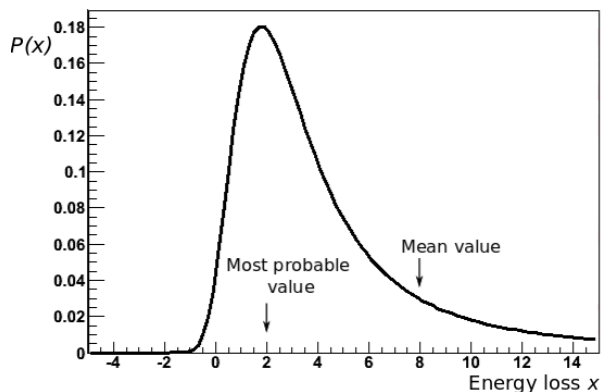
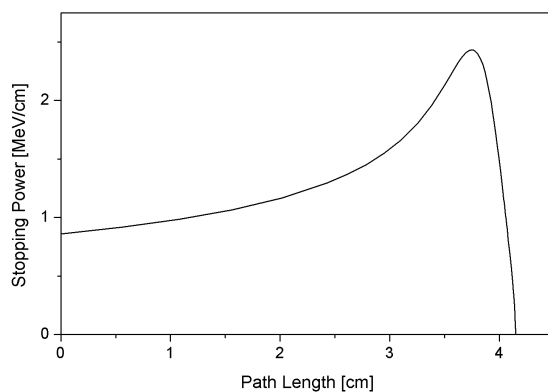Figure 1.4: Landau distribution with most probable values shown.

Figure 1.5: The Bragg curve of 5.49 MeV alpha particles in air. [8]

1.2.2   Electrons

Electrons with laboratory-scale energies primarily come from three effects: β^- decay, internal conversion and Auger electrons.

Beta decay is a nuclear process that can be schematically writen as:

$$^A_Z\mathrm{X} \to\ ^A_{Z+1}\mathrm{Y} + e^- + \bar{\nu},$$
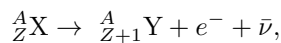
where X and Y are the initial and final nuclear species. The final atom obtains very small recoil energy, which is of no importance in the ionizating radiation topic. The energy spectrum of the outcoming electron is continuous because of the three-body character of the decay. The endpoint energy, which is the maximal possible value of the electron energy spectrum, ranges from a few keV to a few tens of MeV. Neutrinos have very long radiation length (i.e. almost no interaction with matter), thus those coming from the beta decay are of no importance in the ionizing radiation topic.

Internal conversion is a process in which an excited nuclear state deexcites. This happens via an emission of a so called conversion electron. The energy spectrum of these electrons is nearly

monoergetic and ranges from hundreds of keV to MeV. Conversion electron energy spectrum thus consists of several peaks denoting different shell conversions.

Auger electrons appear when an atom is in a state with a vacancy in a normally complete electron shell. This vacancy is then filled with an electron from a higher shell of the atom. This filling in is accompanied with emission of energy which can be emitted either as an X-ray photon or as another electron. These electrons are called Auger electrons and their energetic spectrum is discrete with energies up to a few tens of keV.

Electrons passing through matter lose their energy through two different processes:

◆ Ionization and excitation of atomic electrons

◆ Radiation of a photon – bremsstrahlung

The first case is described by the modified Bethe formula:

$$
-\left(\frac{dE}{dx}\right)_{ion} = \left(\frac{e^2}{4\pi\epsilon_0}\right)^2 \frac{\pi n_e}{m_e c^2 \beta^2} \times
$$
$$
\times \left[\ln\frac{m_e c^2 \beta^2 \gamma^2 T_{\max}}{2I^2} - (\ln 2)\left(2\sqrt{1-\beta^2} - 1 + \beta^2\right) + (1-\beta^2) + \frac{1}{8}\left(1 - \sqrt{1-\beta^2}\right)^2\right],
$$

(1.4)

where the symbols have the same meaning as in Eq. 1.2 [3]. This modified formula describes the collisional losses. However, electrons may also lose their energy through radiative processes, which appear in the form of bremsstrahlung. Bremsstrahlung is a process in which an electron undergoes a gamma-ray emission due to its deceleration when deflected by another charged particle, such as nucleus. The linear specific energy loss for radiative processes is:

$$
-\left(\frac{dE}{dx}\right)_{rad} = \frac{NEZ(Z+1)e^4}{137 m_e^2 c^4}\left(4\ln\frac{2E}{m_e c^2} - \frac{4}{3}\right),
$$

(1.5)

The dependence can be also written as: $dE/dx \sim Z^2/m^3$, which indicates that these losses are only significant in absorber materials with high atomic number. The total linear stopping power is the sum of the collisional and radiative losses. The ratio of the specific energy losses is given by:

$$
\frac{(dE/dx)_{rad}}{(dE/dx)_{ion}} \cong \frac{EZ}{700},
$$

(1.6)

where E is in the units of MeV.

1.2.3 Photons

Laboratory-scale energetic gamma rays can come from many sources. They can be obtained as a result of deexcitation of a beta decay product or nuclear reaction, annihilation radiation, bremsstrahlung or as characteristic X-rays.

Beta decay or nuclear reaction often leave the product nucleus in an excited state and a photon is emitted during its deexcitation with a well defined energy; however, the energy spectrum can be broadened by the Doppler effect for some nuclear reactions. Annihilation radiation are two 0.511 MeV photons moving in the opposite direction that are created as a product of an electron and positron annihilation; positrons can come from e.g. a β^+ decay. Another process, bremsstrahlung, has already been described above; the resulting photons have a low-energy continuous spectrum.

Emission of a characteristic X-ray is a competitive process to the emission of an Auger electron. This happens when a vacancy in an atom shell is filled with an electron from a higher shell. This deexcitation is accompanied with energy emission, its energetic value is determined by the difference
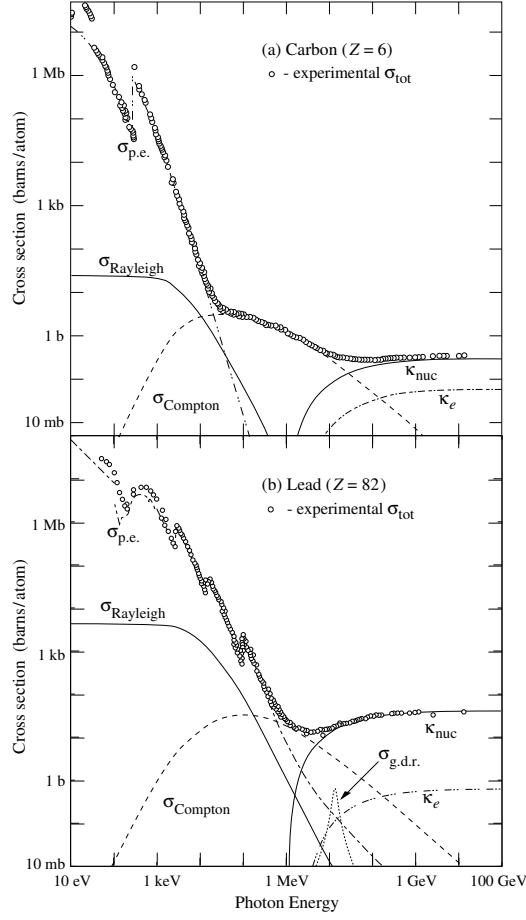
Figure 1.6: Total photon cross section σ_{tot} in carbon and lead, as a function of its energy. [3, 9]

in binding energies of different shells. Quantity called the fluorescent yield is defined as a fraction of the emitted X-rays to all emitted particles, i.e. X-rays and Auger electrons. The X-ray energy spectrum is discrete ranging from 100 eV to 100 keV.

There are three most important interaction mechanisms of gamma rays with matter. The mechanisms are listed below, arranged by the increasing energy of the incoming photon.

◆ Photoelectric absorption

◆ Compton scattering

◆ Electron-Positron $(e^- e^+)$ pair production

The total photon cross section and all its subprocesses as a function of energy is shown in Fig. 1.6, where $\sigma_{p.e.}$ stands for photoelectric effect, $\sigma_{Rayleigh}$ is the Rayleigh scattering, $\sigma_{Compton}$ is the Compton scattering, κ_{nuc} represents the pair production in nuclear field, κ_e is the pair production in electric field and $\sigma_{g.d.r.}$ are the photonuclear reactions, most notably the Giant Dipole Resonance.

In photoelectric absorption, a photon interacts with an absorber atom in a way that the photon is absorbed and a new photoelectron is ejected by the atom. The energy of the ejected electron
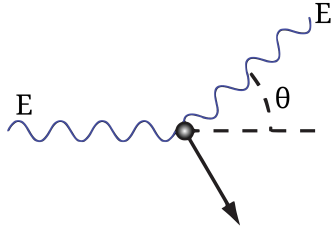
Figure 1.7: The Compton scattering process. [8]

is given by $E_e = E_\gamma - E_b$, where E_γ is the energy of the incoming photon and E_b is the binding energy of the photoelectron in its atomic shell. The probability of this process is $\approx Z^4/E_\gamma^{3.5}$.

Compton scattering (schematics shown in Fig. 1.7) is a process in which an incoming photon of energy E_γ hits an electron at rest, which is then recoiled and the photon is scattered in a different direction at an angle θ with respect to its original direction and different energy E_γ', summing the process $e + \gamma \rightarrow e + \gamma$. Then the energy of the scattered photon is given by:

$$E_\gamma' = \frac{E_\gamma}{1 + \frac{E_\gamma}{m_e c^2}\left(1 - \cos\theta\right)}. \tag{1.7}$$

The probability of Compton scattering is $\approx Z/E_\gamma$. Another type of photon interaction with matter is Rayleigh scattering, which is a coherent scattering, i.e. neither photon nor electron change their energy and only their directions change. An analogy of Compton scattering called inverse Compton scattering exists for electrons. It involves the scattering of low energy photons to high energies by ultrarelativistic electrons so that the photons gain and the electrons lose energy. The name comes from the fact that the participant in this process are opposite of the standard Compton effect.

Pair production $(\gamma \rightarrow e^- + e^+)$ can happen only if E_γ is higher than the rest mass of two electrons (i.e. 1.022 MeV). However, the cross section of this interaction is small for E_γ around 1 MeV, but it becomes dominant for the high energy (of the order of many MeV) photons. During this process, a photon interacts with a nucleus and a pair of electron and positron is created, provided that there is sufficient amount of energy available to create the pair and that both energy and momentum are conserved. Also, this interaction has to happen in the coulomb field of a nucleus so that the momentum conservation law of the process is not violated. The probability of this process is $\approx Z^2 \cdot \ln E_\gamma$.

Electromagnetic shower

Electromagnetic shower (for schematic view see Fig. 1.8) starts when an electron or photon enters an absorber material. High energy photons primarily interact via pair creation, i.e. high energy electron and positron are created. These two then interact through radiating a photon (bremsstrahlung). The cycle continues until either the energy of photons is lower than energy needed for pair production or the pairs are completely stopped in the material.

This property of photons and electrons is employed in the high energy physics (HEP) to determine the energy of incoming particle. Many modern high energy experiments contain an *electromagnetic calorimeter*; its main property is to induce and measure properties of these showers. For example, the calorimeter used in the ATLAS experiment in CERN (for description see Section 2.3.1) is composed of metal plates that act as absorbers and liquid argon that acts as the sensing element.
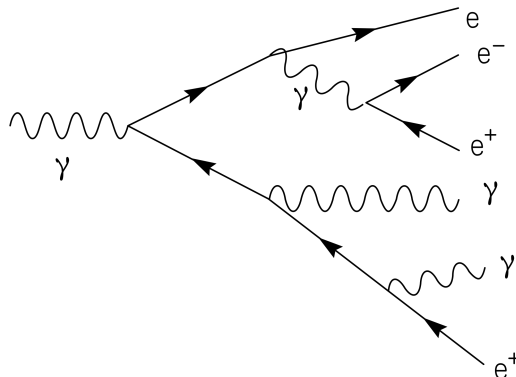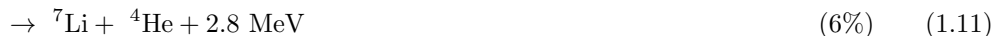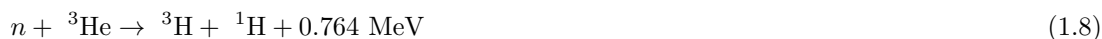
Figure 1.8: Example of the electromagnetic particle shower. [8]

1.2.4   Neutrons

Neutrons are usually produced in (α,n) reactions[4], photoneutron (γ,n) reactions and as a decay result of spontaneous or induced fission. The results of the fission process of a heavier nucleus are besides daughter nuclei also several neutrons with varying energy. Radioisotope (α,n) sources are usually fabricated as a mixture of an alpha-particle emitter combined with an element undergoing (α,n) reaction. This method of obtaining neutrons is also used with gamma-ray emitters combined with appropriate material undergoing (γ,n) reaction. Energies of neutrons obtained this way vary from thermal energies (0.0025 eV) up to a few MeV.

Because of their uncharged nature, most common reactions of neutrons with the surrounding matter are elastic scattering and, over the MeV range, also nuclear reactions. Secondary particles coming from reactions yielding neutrons are in most cases heavy charged particles. This fact has already been described in Section 1.2.1 with an example.

Therefore, two types of detectors are used for neutron detection: reaction-type and recoil-type. The information about neutron's energy is lost in both types. Reaction-type detectors are based on (n,α) or (n,γ) nuclear reactions. The three most common reactions used are:

$$n + {}^{3}\text{He} \rightarrow {}^{3}\text{H} + {}^{1}\text{H} + 0.764 \text{ MeV} \tag{1.8}$$

$$n + {}^{6}\text{Li} \rightarrow {}^{4}\text{He} + {}^{3}\text{H} + 4.79 \text{ MeV} \tag{1.9}$$

$$n + {}^{10}\text{B} \rightarrow {}^{7}\text{Li}^{*} + {}^{4}\text{He} \rightarrow {}^{7}\text{Li} + {}^{4}\text{He} + \gamma(0.48 \text{ MeV}) + 2.3 \text{ MeV} \qquad (94\%) \tag{1.10}$$

$$\rightarrow {}^{7}\text{Li} + {}^{4}\text{He} + 2.8 \text{ MeV} \qquad (6\%) \tag{1.11}$$

Neutron detector is therefore coated with a conversion material (≈ 1 μm thin) that starts the reaction. Recoil-type detectors use elastic scattering: incoming neutron scatters the target nucleus and through the scattering angle an energy deposited per reaction can be determined. Energy of the recoiled nucleus is given as:

$$E_R = \frac{2A}{(1+A)^2} (1 - \cos\theta) E_N, \tag{1.12}$$

where A is the mass number of the target nucleus, E_R is the energy of the recoiled nucleus, E_N is the energy of the incoming neutron, E'_N is the energy of the scattered neutron and θ is the scattering angle of nucleon. The schematics is shown in Fig. 1.9.

---

[4]The nuclear reaction is written in its compact form. A(b,c)D is defined as A + b → c + D.
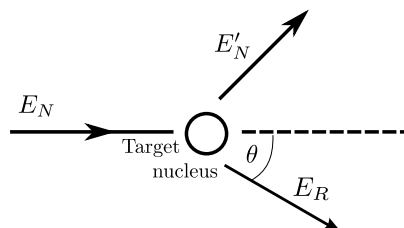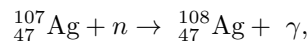
Figure 1.9: Neutron scattering kinematics.

Another neutron detection technique used to determine the neutron flux is activation. This technique is mostly used for the detection of slow neutrons (neutrons with energy smaller than 1 eV). The most commonly used material in this detection method is gold; the undergoing reaction can be denoted as:

$$^{107}_{47}\mathrm{Ag} + n \rightarrow\ ^{108}_{47}\mathrm{Ag} +\ \gamma,$$

where $^{108}_{47}\mathrm{Ag}$ is a β^- emittor. Thin gold plates are irradiated by neutrons and, after some time, from their measured activity, knowledge of the capture cross section, and the target geometry, the neutron flux can be estimated.

1.3 Measurement of radiation

Ionizing radiation has effects on human body which vary with type and energy of radiation. Radiation dosimetry focuses on two areas: description of the radiation beam and measurement and calculation of the absorbed dose.

1.3.1 Characterization of radiation beam

The radiation beam is described by a variable called fluence Φ, which is defined as a the total number of particles N that intersect a unit area A:

$$\Phi = \mathrm{d}N/\mathrm{d}A. \tag{1.13}$$

There are two additional variables used to describe the radiation beam called energy fluence and fluence rate. Energy fluence is defined as a fraction:

$$\Psi = \mathrm{d}R/\mathrm{d}A, \tag{1.14}$$

where R is the radiant energy, $R = \mathrm{d}N \cdot E$ with E being the particle energy. Another variable is fluence rate ϕ, which is defined as the number of particles crossing a unit area per unit time:

$$\phi = \mathrm{d}\Phi/\mathrm{d}t. \tag{1.15}$$

Analogically, a variable called energy fluence rate ψ can be defined:

$$\psi = \mathrm{d}\Psi/\mathrm{d}t. \tag{1.16}$$

The difference in the first two variables and the subsequent ones is that fluence and fluence rate are defined for a monoenergetic beam. However, almost all particle beams are polyenergetic and this notion is reflected in the last two variables.

1.3.2   Characterization of radiation effects on matter

Particle interaction happens in two phases: first, kinetic energy of the ionizing particle is transfered to the charged particles and then the charged particles transfer the energy directly through excitations and ionizations. The initial interaction can be described by a variable called KERMA. The energy retained in the medium is described by a variable called absorbed dose and its variations.

What follows is a list of definitions of different variables used to measure absorbed dose. The unit used with these variables is J·kg^{-1}; however, a special name is used for each variable; this name is denoted in square brackets after the variable name. Table 1.3 shows two different values denoted by a subscript 90 or 07 showing the 1990 and 2007 Recommendations for a system of radiological protection made by the ICRP (International Commission on Radiological Protection, [10, 11]).

KERMA [Gy]

This abbreviation stands for Kinetic Energy Released per unit Mass. KERMA is a measure of the amount of energy transferred from non-ionising radiation (photons and neutrons) into ionising radiation (electrons, protons, heavy charged particles). It is defined as:

$$K = \frac{\mathrm{d}E_{tr}}{\mathrm{d}m}, \tag{1.17}$$

where $\mathrm{d}E_{tr}$ is the sum of the initial kinetic energies of all charged particles liberated by uncharged particles in a mass $\mathrm{d}m$. The medium should always be specified. There are various primary standards to realize K for various particle types and energies.

KERMA in relation to fluence is given as:

$$K = \int \Psi(E) \frac{\mu_{tr}}{\rho}, \tag{1.18}$$

where μ_{tr}/ρ is the tabulated mass energy transfer coefficient of the material for uncharged particles of energy E.

Absorbed dose [Gy]

This variable is defined as:

$$D = \frac{\mathrm{d}\bar{\varepsilon}}{\mathrm{d}m}, \tag{1.19}$$

where $\mathrm{d}\bar{\varepsilon}$ is the mean energy imparted to matter of mass $\mathrm{d}m$. The energy imparted is the sum of all the energy entering the volume minus all the energy leaving the volume, and incorporates any mass energy conversions, e.g. pair production inside the volume will decrease the energy in the volume by 1.022 MeV. The medium should always be specified, since there are again various primary standards to account for various particle types and energies.

Equivalent dose [Sv]

Equivalent dose H_T is defined as:

$$H_T = \sum_R w_R D_{T,R}, \tag{1.20}$$

where w_R is the radiation weighting factor and $D_{T,R}$ is the absorbed dose (averaged over a tissue or organ T) due to radiation of type R. $D_{T,R}$ cannot be measured experimentally. The weighting factor w_R is introduced to weight the absorbed dose for biological effectiveness of the particles (used values are shown in Table 1.3).

Tissue or organ	$w_{T,90}$	$w_{T,07}$
Gonads	0.20	0.08
Bone marrow	0.12	0.12
Colon	0.12	0.12
Lung	0.12	0.12
Stomach	0.12	0.12
Breast	0.05	0.12
Bladder	0.05	0.04
Liver	0.05	0.04
Oesophagus	0.05	0.04
Thyroid	0.05	0.04
Skin	0.01	0.01
Bone surface	0.01	0.01
Salivary glands	–	0.01
Brain	–	0.01
Remainder	0.05	0.12
Whole body total	1.00	1.00

Type and energy of radiation R	$w_{R,90}$	$w_{R,07}$
Photons, all energies	1	1
Electrons and muons, all energies	1	1
Protons > 2 MeV	5	2
Neutrons		
< 10 keV	5	
10 to 100 keV	10	
> 0.1 to 2 MeV	20	See text
> 2 to 20 MeV	10	
> 20 MeV	5	
Alpha particles, fission fragments, heavy nuclei	20	20

Table 1.3: Examples of the radiation weighting factor w_R (left) and the tissue weighting factor w_T (right). [10, 11]

As can be seen in the Table, the recommendations vary. The 1990 recommendation was defined for protons with energy higher than 2 MeV, whereas the $w_{R,07}$ is for all energies of protons and charged pions. However, the biggest change is in the neutron weighting factor, which is now a continuous function of energy defined as:

$$
w_R = \begin{cases}
2.5 + 18.2e^{-[\ln E_n]^2/6} & \text{if } E_n < 1 \text{ MeV} \\
5.0 + 17.0e^{-[\ln 2E_n]^2/6} & \text{if } 1 \leq E_n \leq 50 \text{ MeV} \\
2.5 + 3.25e^{-[\ln 0.04E_n]^2/6} & \text{if } E_n > 50 \text{ MeV}
\end{cases}
\tag{1.21}
$$

where E_n is the energy of radiation neutron.

Effective dose [Sv]

This variable is defined as:

$$
H = \sum_T w_T H_T = \sum_T w_T \sum_R w_R D_{T,R},
\tag{1.22}
$$

where w_R is the radiation weighting factor, $D_{T,R}$ is the absorbed dose defined above and w_T is a tissue weighting factor which reflects the total detriment to health. Recommended values of the weighting factor can be found in Table 1.3.

Semiconductor detectors

This chapter is dedicated to the introduction to semiconductors and their applications. Firstly, semiconductor materials and their properties are presented along with the definition and some applications of a p-n junction. Next, the usage of semiconductors as detectors is examined. The largest part of this section is devoted to the silicon position detectors with emphasis on pixel detectors and concludes with a real-life example, the pixel detector used at ATLAS experiment in CERN.

2.1 Semiconductor materials

Solid materials can be divided into three groups: conductors, semiconductors and insulators. The difference between these three types is in the distance of their valence and conductive band called band gap. [1] For insulators, the width is around 6 eV, i.e. there is minimal chance for electrons to pass from the valence band and become conductive. In conductors these bands overlap. Last but not least, the gap size in semiconductors is approximately 1 eV, which means that very few electrons gain enough thermal energy to leap the band gap at the room temperature, but their electrical properties can be controlled via other ways than thermal excitation.

The focus of this work is on silicon semiconductor detectors, therefore the list of elementary silicon properties is shown in Table 2.1.

Even at room temperature, some electron-hole pairs are created. The probability of the generation of one pair per unit time is given by:

$$p(T) = CT^{3/2} \exp\left(-\frac{E_g}{2kT}\right),\tag{2.1}$$

where T is the absolute temperature, E_g is the bandgap energy, k is the Boltzmann constant and C is the proportionality constant characteristic to the material. Once created, both electron and hole start to move away from their point of origin in random direction. This movement is called diffusion. The distribution of the floating charges in time is a broadening Gaussian function with a standard deviation given by $\sigma = \sqrt{2Dt}$, where D is the diffusion coefficient and t is the elapsed time. The diffusion coefficient can be described as:

$$D = \mu\frac{kT}{e},\tag{2.2}$$

where μ is the mobility of the charge carrier, k is the Boltzmann constant, T is the absolute temperature and e is the electrical charge of an electron.

Atomic number	14
Atomic weight	28.08
Atomic density	$4.99 \cdot 10^{22}$ cm^{-3}
Stable isotope mass numbers	$28 - 29 - 30$
Density (300 K)	2.33 g/cm^3
Dielectric constant	11.7
Forbidden energy gap (300 K)	1.12 eV
Forbidden energy gap (0 K)	1.17 eV
Electron mobility (300 K)	1350 cm^2/(V$\cdot$s)
Hole mobility (300 K)	480 cm^2/(V$\cdot$s)
Electron mobility (77 K)	1350 cm^2/(V$\cdot$s)
Hole mobility (77 K)	480 cm^2/(V$\cdot$s)
Electron diffusion constant	34.6 cm^2/s
Hole diffusion constant	12.3 cm^2/s
Intrinsic carrier density (300 K)	$1.45 \cdot 10^{10}$ cm^{-3}
Intrinsic resistivity (300 K)	235 kΩcm
Melting point	1415 $^\circ$C
Thermal expansion coefficient	$3 \cdot 10^{-6}$ K^{-1}
Breakdown field	30 V/μm
Energy required for creation of a single e-h pair (77 K)	3.76 eV
Energy required for creation of a single e-h pair (300 K)	3.60 eV

Table 2.1: The physical properties of silicon. [12, 13]

When an external electric field is applied to the semiconductor material, both electron and hole start to move. The motion will be a combination of thermal diffusion motion plus drift velocity parallel to the direction of the applied field. At low values of electric field intensity, the drift velocity v is proportional to the magnitude of the field, thus giving a relation:

$$v_e = \mu_e \epsilon, \quad v_h = \mu_h \epsilon, \tag{2.3}$$

where μ is a mobility for electrons or holes and ϵ is the electric field magnitude. In silicon, the mobility of electrons is approximately equal to three times the mobility of holes. For higher electric field intensities, the velocity rises slowly until it reaches a saturation velocity which does no longer change with increasing intensity. The saturated velocities are of the order of 10^7 cm/s. [1]

2.1.1   Types of semiconductors

There are three types of semiconductors which vary in the type of impurities: intrinsic, n-type and p-type. A new variable called resistivity is introduced to better describe the properties of semiconductors:

$$\rho = \frac{AV}{Id} = \frac{1}{en_i(\mu_e + \mu_h)}. \tag{2.4}$$

Resistivity ρ is defined for a semiconductor with thickness d and a surface area A through which current I will flow when a voltage V is applied across the thickness. The second part of the equation uses the electron charge e, the intrinsic carrier density n_i and the mobility of electrons and holes.

In an intrinsic detector, the number of electrons in the conduction band is exactly the same as the number of holes in the valence band. This is typically denoted as $n_i = p_i$, where n is the concentration of electrons in the conduction band and p is the concentration of holes in the

<div align="center">(a)   (b)</div>
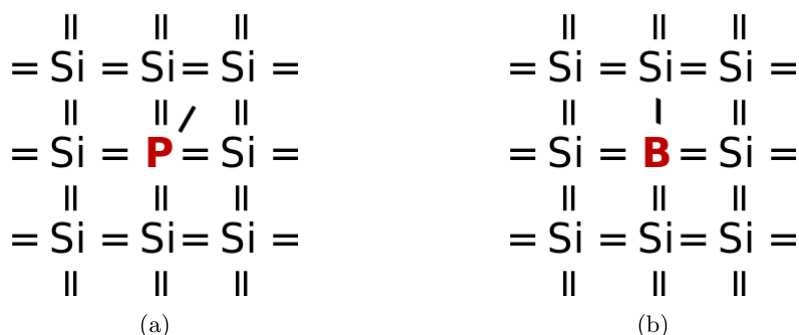
Figure 2.1: Types of impurities in semiconductors: donor impurity (left) and acceptor impurity (right). The lines indicate the valence electrons of the atoms.

valence band. This condition implies that it is impossible to produce intrinsic detectors (due to residual impurities), but they are of theoretical importance. Resistivity of intrinsic silicon at room temperature is $\rho = 2.3 \times 10^5 \ \Omega \cdot \text{cm}$ [1].

In a n-type or p-type semiconductor, a dopant is added to an intrinsic semiconductor to change its properties. In the case of n-type detector, the impurities are called donors. The elements used are usually phosphorus (P) or arsenic (As) from the group V with five valence electrons. The scheme of this process is shown in Fig. 2.1a – the donors contribute extra electrons to the conduction band, thus making the electrons the majority charge carriers and the holes the minority charge carriers. The equilibrium concentration of holes and electrons is independent of the doping concentration and is given as an equivalent to the constant given by the intrinsic silicon: $np = n_i p_i$. The resistivity of a n-type semicondutor is given as:

$$\rho = \frac{1}{en\mu_e}. \tag{2.5}$$

For the concentration of electrons $n = 10^{13}/\text{cm}^3$ the resistivity of silicon will be $\rho = 500 \ \Omega \cdot \text{cm}$. [1]

The impurities in a p-type material are called acceptors (scheme in Fig. 2.1b). The elements used in this case are for example boron (B) or aluminium (Al) from group III, which have three valence electrons. In a p-type material, the majority carriers are holes and the minority carriers are electrons.

In case of heavily doped thin layers of semiconductor, a special notation is used: n^+ and p^+ for n-type and p-type semiconductors, respectively.

2.1.2   The p-n junction

After joining of a p-type and n-type crystal together a p-n junction forms at their interface. This is just a simplified explanation, because it is impossible to create a p-n junction just by adding two crystals together. After joining p-type and n-type semiconductors, a diffusive diffusion of majority carriers across the junction appears. The regions nearby the p–n interface lose their neutrality and become charged, forming a depletion layer (see Fig. 2.2). The barrier created by the migration of charge carriers stops further migration and is called the built-in potential being of the order of a few hundred milivolts.

A semiconductor diode can be constructed from a p-n junction. This electronic component functions in two modes. In the first one, when the diode is forward biased, the current flow is permitted in the electrical circuit. In the second mode, the diode is reversed biased, which translates into no current flow in the circuit.
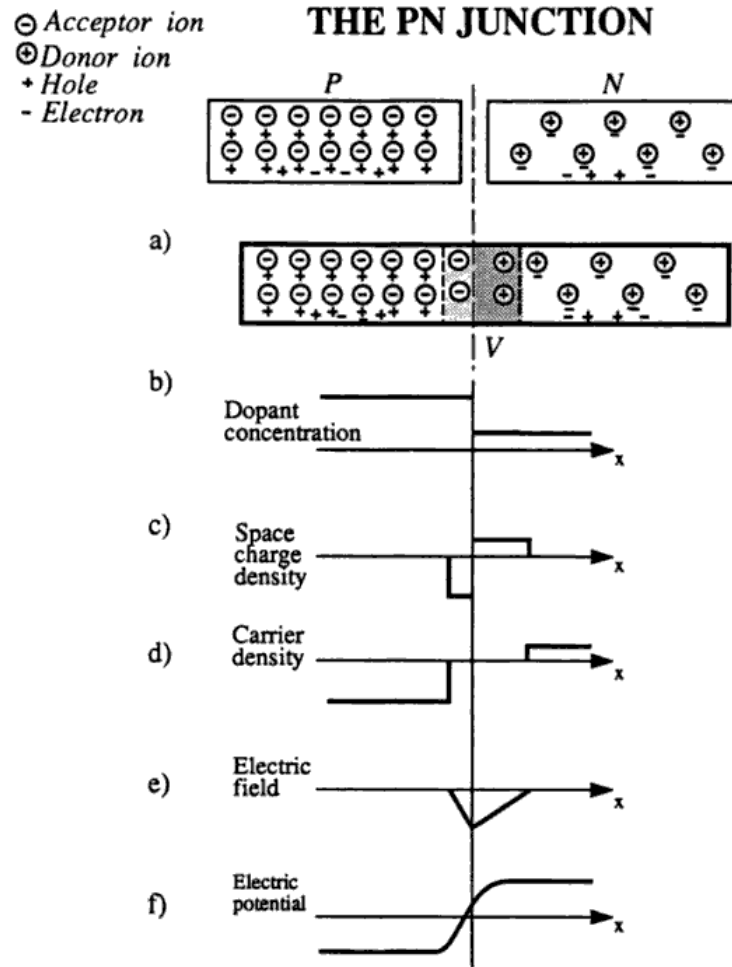
<div align="center">19</div>

Figure 2.2: The p-n junction. a) Two crystals of opposite type are brought together and a depletion layer is formed on either side of the junction. b) The dopant concentration. c) Net space charge density showing zero charge except for a dipole layer at the junction. d) Electron and hole density through the crystal showing no free carriers in the depleted zone. e) Electric field distribution. f) The potential distribution within the depletion region. [12]

The distribution of the electric potential φ can be computed via solution of the Poisson equation:

$$\nabla^2 \varphi = -\frac{q_d}{\varepsilon}, \tag{2.6}$$

where ε is the dielectric constant of the medium and q_d is the space charge density. For one dimensional problem the equation becomes:

$$\frac{\mathrm{d}^2 \varphi}{\mathrm{d}x^2} = -\frac{q(x)}{\varepsilon}, \tag{2.7}$$

which can be solved with double integration and boundary conditions. The space charge density is shown in Fig. 2.2c and can be denoted as:

$$q(x) = \begin{cases} eN_d & (0 \leq x < x_1) \\ -eN_a & (-x_2 < x \leq 0) \end{cases} \tag{2.8}$$

where N_d and N_a are donor, resp. acceptor concentrations. The equilibrium condition must still hold, which translates as $x_1 N_d = x_2 N_a$. The electric field E is defined as $E = -\nabla\varphi$. The boundary condition given by the electric field is $E(-x_2) = E(x_1) = 0$. The solution for the electric field takes the form:

$$E(x) = \begin{cases} -\frac{eN_d}{\varepsilon}(x + x_1) & (0 \leq x < x_1) \\ \frac{eN_a}{\varepsilon}(x - x_2) & (-x_2 < x \leq 0) \end{cases} \tag{2.9}$$

This behaviour is shown in Fig. 2.2d. Another integration and application of boundary conditions $\varphi(x_1) = V$, $\varphi(-x_2) = -V$ yields the result:

$$\varphi(x) = \begin{cases} -\frac{eN_d}{2\varepsilon}(x + x_1)^2 + V & (0 \leq x < x_1) \\ \frac{eN_a}{2\varepsilon}(x - x_2)^2 - V & (-x_2 < x \leq 0) \end{cases} \tag{2.10}$$

The electric potential distribution is shown in Fig. 2.2e.

The depletion zone width ($W = x_1 + x_2$) can be expanded by applying an external reverse-biased voltage (bias voltage, V_B). The depletion zone width is given as:

$$W = \sqrt{2\varepsilon\rho\mu V_B}, \tag{2.11}$$

where ε is the dielectric constant, ρ is the material resistivity and μ is the majority carrier mobility.

The best signal-to-noise ratio is reached in fully depleted semicondutors. The background is caused by the thermally generated minority charge carriers. Under equilibrium conditions (no external forces such as voltages, electrical fields, magnetic fields, or temperature gradients are acting on the semiconductor), electron-hole pairs are generated throughout the volume, and without an external voltage these carriers recombine. However, if an electric field is present, the pairs are separated and drift in opposite directions. This drift gives rise to a so called leakage or reverse current.

2.1.3   Metal-Oxide-Silicon structure

A thin silicon oxide layer sandwiched between a conductive plate and a silicon substrate is called the Metal-Oxide-Silicon (MOS) structure. However, this composition is not the only possible one; the oxide may be replaced with any suitable insulator and the material used for the metallic part is usually polysilicon. The cross section of such structure is shown in Fig. 2.3a. Ordinarily, pixel detectors are directly coupled to the readout electronics using these structures.

metal

oxide

silicon substrate

ohmic contact

(a)

EMITTER   BASE   COLLECTOR

I_E p^+ n p I_C

I_B

$+$ $-$ $+$ $-$

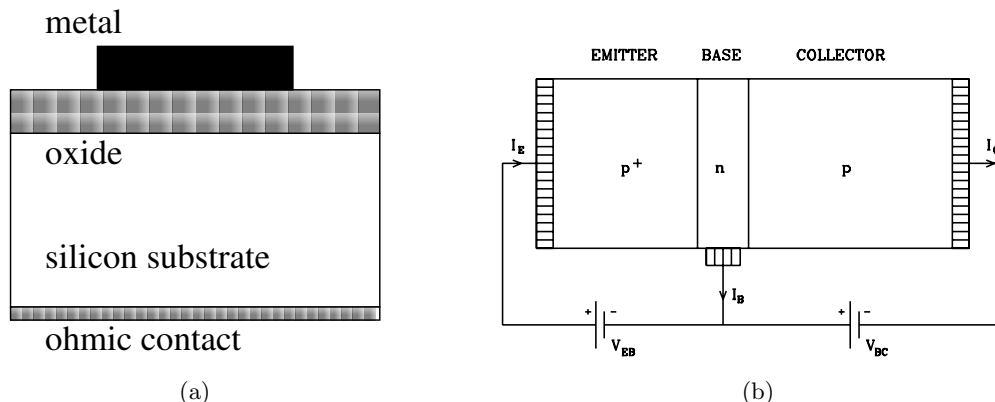V_{EB} V_{BC}

(b)

Figure 2.3: Schematic cross section of a MOS structure (left, [14]) and of a bipolar transistor (right, [15]).

There are several operating states of the MOS structure: flat band condition, accumulation, depletion and inversion. Flat band condition is a state when no external voltage is applied and, since the oxide is taken to be a perfect insulator with no charge centers, both metal and silicon layer reach thermal equilibrium. Accumulation is a situation in which a negative voltage with respect to the charge of the silicon bulk is applied to the metal, e.g. in the case of p-type silicon, negative voltage is applied. In this case, the charge carriers are attracted to the oxide layer, and as a result the voltage appears across the oxide layer. If the opposite sign of the voltage is applied, e.g. positive voltage is applied to the structure for a p-type silicon, the carriers are pushed away from the oxide layer and form a depletion zone, thus giving this situation the name depletion. Inversion happens when thermally generated pairs of holes and electrons in silicon traverse to their respective charged side. A thin layer of charge carriers is then formed near the oxide layer with charge inverse to the one of the silicon bulk.

2.1.4 Transistor

The final detector consists not only of the sensor itself, but also the connecting and readout electronics must be considered. Transistor is a semiconductor device and a fundamental building block of modern electronic devices, so it can be commonly found in the readout electronics. It was invented in 1947 and the inventors were awarded the Nobel prize for their work in 1956 (more details can be found in Ref. [16]).

Transistors can be used either as switches or as amplifying devices. They are classified into two groups: unipolar, where only one charge carrier type participates in the current flow, and bipolar, where both types of charge carriers participate. The bipolar transistors were the most common type of transistors in the 1960's and 70's mostly, but as the integrated circuit technologies matured, the unipolar transistors (mostly MOSFETs) took most of the market share.

2.1.4.a   Bipolar transistors

Bipolar transistor consists of two back-to-back p-n junctions with a common base. Fig. 2.3b shows a schematics of a p-n-p transistor. The terminals of a bipolar transistor are labeled *emitter*, *base* and *collector*.

In order to have good amplifying properties, a transistor must meet these three requirements: the doping concentration of the emitter has to be large with respect to the base, the base must be
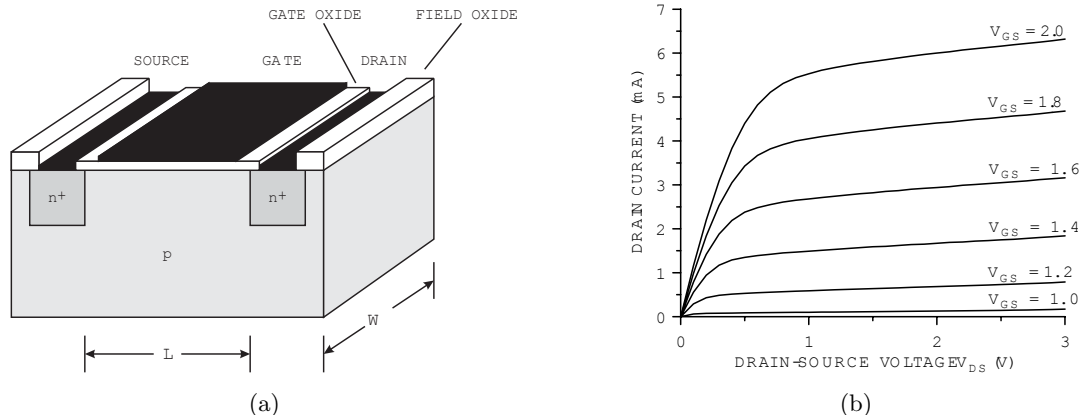
Figure 2.4: Schematic cross section of a MOS transistor (left) and a measured MOSFET current-voltage characteristic (right). [17]

very thin, and the doping concentration of the collector should be small. The sizes of the terminals indicate that the emitter and collector currents are relatively the same size. The currents flowing in and out of the transistor follow the Kirchhoff's current law: $I_B = I_E - I_C$, which means that whenever a small current flows into the base, a larger current flows from the emitter to the collector, effectively resulting in yielding a high collector current from a relatively small base current. Voltage gain mode is also possible.

2.1.4.b   FET transistors

Unipolar transistors are called the field-effect transistors (FET). Electrons are used for conduction in a n-channel FET and holes in a p-channel FET. The terminals of the FET are labeled *source*, *gate*, *drain*, and *body* (substrate). In this type of transistor, gate voltage can control a current between source and drain. Drain and source are connected by a conductive layer in the area below the gate called a channel.

MOSFETs are a type of transistors in which the conductive gate is insulated from the body with a thin oxide layer. MOSFET is esentially a combination of a MOS structure with a FET transistor and a schematic cross-section is shown in Fig. 2.4a. This combination allows almost no current consumption at the gate due to the insulating layer.

A p-channel MOSFET, or PMOS, is a MOSFET in which the source and drain are p-type, and the substrate is n-type. Likewise, a NMOS is a MOSFET with the source and drain of n-type and the substrate of p-type.

Several characteristics of the MOS transistors can be studied. One of them is the current-voltage characteristic, which is a plot of the drain-source current versus drain-source voltage. An example of such a characteristic is shown in Fig. 2.4b. A curve is plotted for different gate-source voltages. Two sections of the dependencies can be distinguished: a linear section and for a higher gate-source voltage a saturation section. In the linear region the MOSFET acts as a resistor; in the saturation region, the drain-source voltage only slowly rises and resembles saturation behavior. The transistor exhibits a finite output resistance in this region. If a FET is used as an amplifier, it will be most probably operated in this region, since it provides maximum voltage gain.

Another important characteristic of MOS transistors is the threshold voltage. During its operation, the transistor goes from weak to strong inversion. The gate voltage at which this transition happens is defined as the threshold voltage. Below this value, in the weak inversion, the drain

23

current increases exponentially with the gate voltage. Above this value, the current raises more gradually.

The dependence of the drain-source current I_{DS} on the gate and threshold voltage can be described as:

$$I_{DS} \approx \frac{W}{L} \mu \left(V_{GS} - V_{TH} \right)^2,$$ (2.12)

where W and L are the channel width and length, μ is the mobility of the carriers in the channel, V_{GS} is the gate-source voltage and V_{TH} is the threshold voltage.

2.2   Technology of fabrication of silicon sensors

In order to produce a detector grade silicon, several steps must be taken. Firstly, an ingot of enough purity is prepared via a feasible way; explanation of the common ways follows in this section. Next, the ingot is sliced into wafers and then further processed. This is a multistep process which is also described later.

2.2.1   Silicon crystal growth techniques

Even though silicon is a quite common chemical element found on Earth (it makes up 27.7 percent of Earth's crust [18]), the properties of silicon that can be obtained from nature are not 'pure' enough to pass as a radiation detection sensor. Therefore a special pure silicon ingots have to be grown. These finished ingots are then cut into wafers and further processed (see the next section). Three growth techniques will be described: the Czochralski method, the float zone method and the epitaxial technique. Silicon created with any of these methods fulfils the requirements set for a silicon particle detector: high resistivity and high carrier lifetime. Produced ingots are then sliced into wafers which are processed further.

This section is heavily based on the Ref. [19] and the references therein.

2.2.1.a   Starting material

The first step in the production of silicon ingots is obtaining silicon through mining of silicon dioxide in the form of a very pure sand. Silicon dioxide is then melted in the presence of carbon at a furnace at a temperature of about 1780 °C. The main undergoing process is:

$$SiO_2 + 2C \rightarrow Si + 2CO.$$
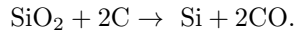
At this stage, silicon is already 99% pure. Once the liquid cools to a solid, the result is called Metallurgical Grade Silicon (MGS). The MGS is then ground into a fine powder which is converted into trichlorsilane with the help of hydrogen chloride gas:

$$Si + 3HCl \rightarrow SiHCl_3 + H_2.$$
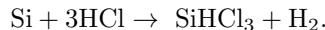
This step is implemented to rid the mixture of electrically active impurities until their concentration is under 1 ppb via multiple distillation. The polysilicon is then deposited on a hot silicon rod where the last equation is reversed. The resulting silicon is called the Semiconductor Grade Silicon (SGS). At this stage, the concentration of electricaly active impurities in the SGS are as follows[1]: phosphorus, boron and arsenic concentration are $\approx 1 \times 10^{11}$ cm^{-3}, carbon concentration is $\approx 2 \times 10^{15}$ cm^{-3} and oxygen concentration is below 5×10^{14} cm^{-3}.

---

[1]All concentration values stated in this section come from [19]. As stated there, the values come from a private communication; the only publically listed values of impurities is e.g. a 99.9999999% purity level [20].
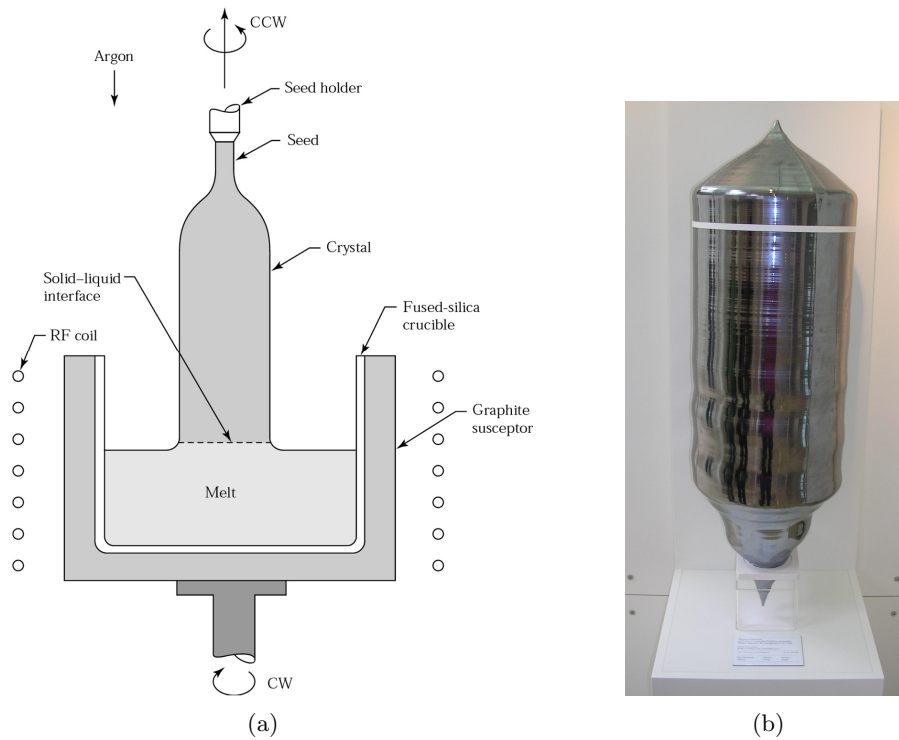
Figure 2.5: Schematic setup of a Czochralski crystal puller (left, [21]). Single silicon crystal produced with the Czochralski method (right, [8]).

2.2.1.b   Czochralski process

The Czochralski method is named after J. Czochralski, who published an article in 1918 about "A new method for the measurement of the crystallization rate of metals" [22]. This pull-from-melt method has been used for the production of single semiconductor crystals since 1950. Schematic setup of the Czochralski method is shown in Fig. 2.5a.

Firstly, a polysilicon material is melted in a quartz crucible (SiO_2) at a temperature of about 1400 °C and a single crystal seed is inserted into the melt to start the crystal growth process. The seed crystal is then slowly withdrawn and slowly rotated so that the molten silicon crystallizes to the seed. The melt temperature, rotation rate and pull rate are all important parameteres of the process. For example, the diameter of the final ingot is controlled this way; once the desired diameter is achieved, the crystal is pulled faster to maintain the shape. The expanding part of the crystal from the seed to the final diameter is called the neck of the crystal. This method is performed in an inert gaseous atmosphere.

The final ingot is a large continuous crystal extending from the seed with the same orientation. The final diameter differs based on the application and the length can be up to 2 m, which is then sliced into single wafers. A Czochralski ingot can be seen in Fig. 2.5b; it is displayed in Deutsches museum, Munich, Germany.

The drawback of this method is that as the liquid silicon is contained in a crucible during growth, the impurities from the crucible are incorporated into the crystal. The two most important impurities are carbon and oxygen. Carbon concentration is $\approx 5 - 50 \times 10^{15}$ cm^{-3} and the one of oxygen is $\approx 5 - 10 \times 10^{17}$ cm^{-3}.
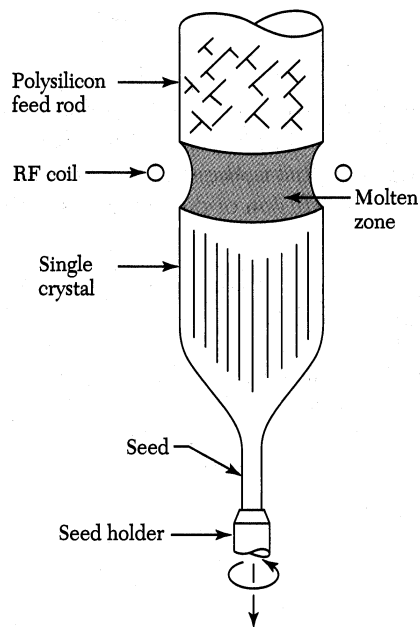
Figure 2.6: Schematic view of the float zone method. [21]


2.2.1.c   Float zone process

An advantage of the float zone method over the Czochralski one is smaller concentration of impurities in the finished crystal. However, disadvantages are higher price for manufacturing and also diamater limitations of the final ingot. Using the Czochralski method, diameters up to 450 mm can be produced, whereas the biggest crystals made with the float zone method have 150 mm diamater at maximum.

The float zone method (FZ) was invented in 1962 by Theuerer [23], and it is based on a zone-melting principle. The schematics of this method can be seen in Fig. 2.6. A cylindrical polysilicon rod is connected to a monocrystalline seed crystal at the lower end. Both are melted with a radio frequency field (RF). As the RF coil moves upwards, below the molten area a solid single crystal ingot is formed. The impurities contained in the polysilicon rod preffer to stay in the melt because of their small segregation coefficients. Segregation coefficient denotes the relation between the concentration of impurity atoms in the growing crystal and that of the melt. Their small values result into a purified silicon ingot with low impurity concentrations. The carbon and oxygen concentration is below 5×10^{15} cm^{-3}. This method takes place in a vacuum or an inert gaseous atmosphere.

Disadvanteges of this method come from its geometry – it is very difficult to keep larger amounts of molten silicon from collapsing. Also, the price is higher than for crystals made with the Czochralski method.

FZ crystals are doped by adding a doping gas to the processing chamber. For a n-type semiconductor, phosphine (PH$_3$) is added, and for a p-type semiconductor, diborane (B$_2$H$_6$) is used. Due to its small segregation coefficient, phosphorus cannot be segregated, and moreover, it quickly evaporates from the melt, whereas due to the value of boron segregation coefficient, no purification of n-type FZ can be reached. This means that it is easier to produce a more homogenous p-type FZ than an n-type FZ.

To achieve better homogeneity of high resistivity n-type silicon, a neutron transmutation doping method is used. In this case, a high purity p-type FZ ingot is subjected to a neutron bombardment in a reactor. Part of ^{30}Si ($\approx 3.1\%$ of silicon) atoms undergoes a reaction in which they form an unstable isotope ^{31}Si which then decays with a half-life of 2.62 hours to a stable phosphorus isotope ^{31}P via β^- decay. The nuclear reaction can be schematically written as:

$$^{30}_{14}\text{Si} + n \rightarrow^{31}_{14}\text{Si} + \gamma \rightarrow^{31}_{15}\text{P} + \beta^- + \nu.$$
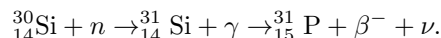
The resulting crystal is then annealed at about 800 °C for defect annihilation and activation of the phosphorus dopant. Thus a high resistivity homogeneous p-type silicon can be processed into high resistivity n-type silicon with such a homogeneity that is not possible with standard FZ doping.

2.2.1.d Wafer production and processing

The first step in wafer production is to remove the seed and the other end from the silicon ingot. The resulting cylinder is then grinded to obtain a unified diameter all over the ingot. The next step is flat grinding. Two types of flats are produced: the primary flat, which is the largest, allows a mechanical locator in the automatic processing equipment to position the wafer, and the secondary flats, which define the orientation and conductivity type of the crystal.

The ingot is then sliced into wafers either by wire sawing or by diamond blade sawing. Both processes result in some loss of silicon due to the creation of a silicon saw dust.

The next step of wafer processing is chemical etching, which removes sawing damage. The final step is of wafer shaping is polishing. Its purpose is to provide a smooth, specular surface where device features can be defined by lithographic processes.

2.2.1.e Epitaxial silicon

Epitaxial growth is the process of depositing a thin layer (0.5 to 20 μm) of single crystal material over a substrate wafer. Epitaxial layer can be grown at temperatures below the melting point (typically below $30 - 50\%$ [21]), which is a difference from the previously described melt-growth techniques.

Epitaxy is commonly done via a vapor-phase epitaxy (VPE), in which a low resistivity silicon wafer acts as a seed on which compound silicon gases are deposited. The four mainly used chemical compounds are: silicon tetrachloride ($SiCl_4$), trichlorosilane ($SiHCl_3$), dichlorosilane (SiH_2Cl_2), and silane (SiH_4). Among these compounds, tetrachloride is the one most widely used and studied.

The over-all reaction for the hydrogen reduction of tetrachloride to form a silicon epitaxial layer is as follows:

$$SiCl_4 + 2H_2 \rightarrow Si + 4HCl.$$
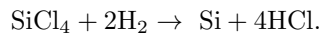
On the right side of the reaction, there are two gases that form a solid silicon and a gas product. The typical reaction temperature is around 1200 °C. However, another competing reaction takes place reducing the solid silicon growth rate:

$$SiCl_4 + Si \rightarrow 2SiCl_2.$$
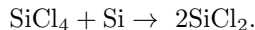
A typical growth rate lies in the order of 1 μm/min.

To create p-type or n-type layers, it is possible to add gaseous phosphine (PH_3) or diborane (B_2H_6) to the compound silicon gas.
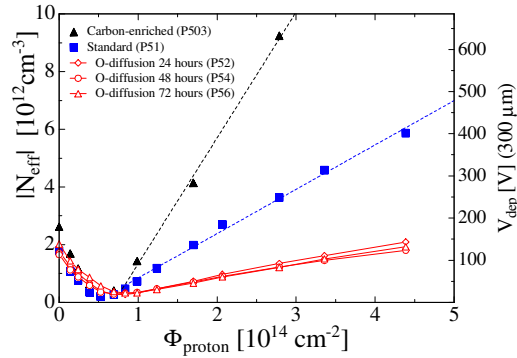
Figure 2.7: Influence of carbon and oxygen impurities on the depletion voltage V_{dep} as a function of the proton fluence Φ_{proton}. [24]
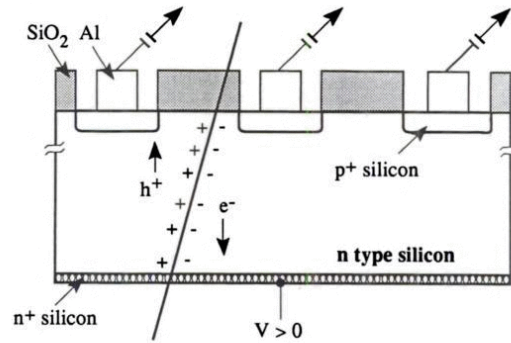

Figure 2.8: Cross-section of a silicon particle detector. [12]

2.2.1.f Defect engineering

It is impossible to create a silicon wafer without impurities. However, it has been shown that impurities can enhance some wanted properties, such as radiation hardness. Thus, defect engineering, a study of the effects of artificially added impurities to the detector, came to terms. The standard concentrations of oxygen or carbon in silicon detectors were mentioned above in the appropriate sections.

Since the oxygen and carbon impurities act as trapping centers of the primary radiation induced vacancies and interstitials, a question has been raised whether silicon with enriched impurities concentration would be more radiation hard. An answer is visible in Fig. 2.7 by ROSE collaboration. Silicon created using the DOFZ (Diffusion Oxygenated Float Zone) method was used in this analysis. In this method, oxygen is diffused into the silicon bulk at high temperatures (around 1100 °C) using the silicon-oxide layer as the source of the oxygen. The results show that the increased oxygen content is beneficial for lessening of the damage caused by charged hadron irradiation, whereas the increased carbon content worsens the properties of the used material with respect to the standard silicon. [24]

2.2.2   Silicon processing

The fabrication technology of silicon detectors is derived from the planar technology developed in the field of microelectronics. A minimum feature size of the photolithographic process used for

n - Si

SiO^2

Oxide passivation

Opening of windows

Doping by ion implantation

B	:	15 keV	5×10^{16}	cm^{-2}
As	:	30 keV	5×10^{15}	cm^{-2}

p$^+$

Annealing at 600 °C, 30 min

n+   AL

Al patterning at the front

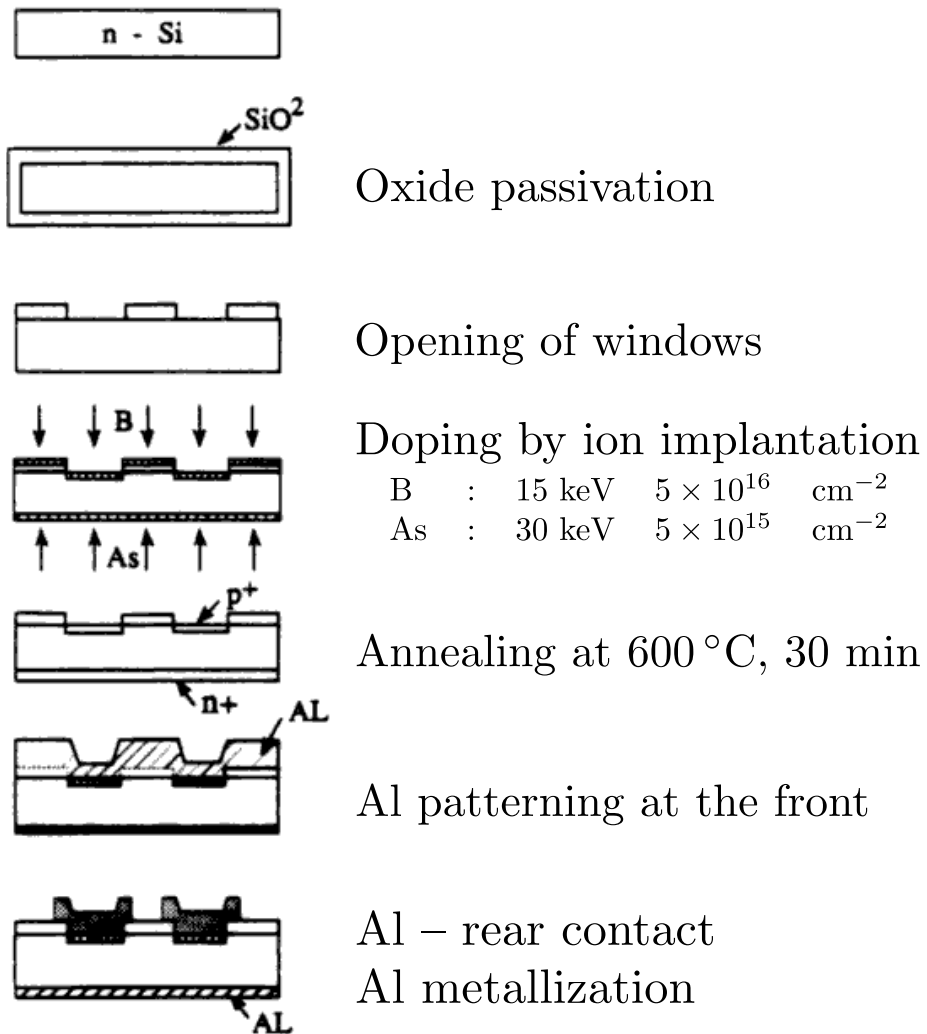Al − rear contact
Al metallization

AL

Figure 2.9: The planar process for detector fabrication. The dimensions are not to scale. [12]

sensor fabrication is usually larger compared to the typical size of microelectronics chip. However, for a processing of detectors, specific requirements must be taken into account that have not been covered in the planar technology. The specific requirements of silicon detectors are: high purity of silicon, both sides of wafer available for processing and large areas without defects. Some of the requirements have been described in the previous section on silicon production.

Example of a silicon strip sensor is shown in Fig. 2.8. A high purity n-type silicon has a highly doped n^+ silicon layer on one side and strips of p^+ silicon on the other. Every p^+ strip is metallized to allow ultrasonic bonding of strips to the electronics. The surface of the detector is covered with passivation oxide for mechanical protection.

The individual stages of processing are shown in Fig. 2.9. In this case, the outcome will be a p^+-n-n^+ detector; however, p^+-i-n detectors are also fabricated (see Section 2.6 in Ref. [14] for their processing).

The first step is the thermal oxide passivation of the silicon wafers which serves to protect the wafer surface with a thin layer of SiO_2. The thin layer is achieved by storing the wafer at a temperature between 900 and 1200 °C in an oxygen atmosphere. Next, windows need to be open in the oxide to enable the ion implantation in the desired areas. This is achieved through litographic and etching techniques. The first step is deposition of a thin layer of photoresist. The photoresist is then illuminated through a photolitographic mask defining the desired pattern. The illuminated regions of the photoresist are etched away in the following process step.

The next step, doping, is done either by implantation (shown in the aforementioned figure) or by diffusion. Fig. 2.9 shows typical values of ion energies and densities in implantation. The advantage of this process is its reproducibility – the implantation dose can be precisely measured. Also, since this process is performed at room temperatures, the photoresist mask can be used to mark the areas not to be doped. Diffusion, on the other hand, is affected by the gradient of the concentration: most dopant can be found at the surface. The dopants enter the wafer at a temperature of 800 to 1200 °C. This temperature is too high for the photoresist, thus the wafer has to be protected with an oxide layer. Next step is annealing at 600 °C for 30 minutes, which serves to reduce the damage caused by the irradiation with heavy ions and to diffuse the dopants further from the surface.

The doped wafers are then metallized to provide a low resistivity connection, because bonding is possible only on metals. A typical thickness is 1 μm. The surface of the wafer is then covered with aluminium and the desired pattern is achieved using appropriate masks. The wafer is then ready for cutting.

2.3   Types of semiconductor position sensitive detectors

In this section, semiconductor position-sensitive detector types will be presented. The materials used for fabrication of these detectors vary. Many different materials are used for detector fabrication. The most often used material is Si, but other than that Ge, CdTe, or SiC are also used. The choice of a material depends on the field of application, detector efficiency and sensitivity or other detector properties.

These detectors are currently widely used in high energy physics (HEP) experiments. Thus in the last part of this section, an example of an experiment from this field, which uses silicon position detectors, is presented.

Strip detectors

Strip and pixel detectors are often categorised together. The convention has it that if the dimensions of the individual electrodes are of the size of 1 mm or larger, then they are called strip detectors (devices with smaller electrodes are called pixels). The measurement precision of binary readout
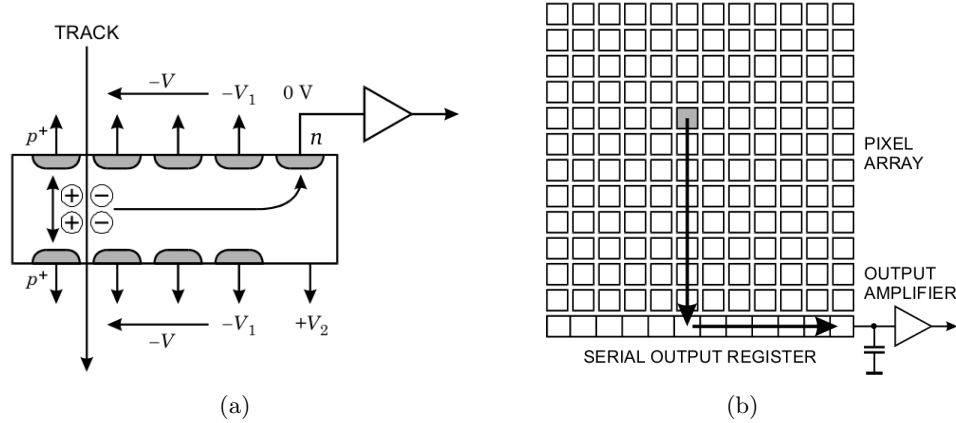
Figure 2.10: Structure of a silicon drift detector (left). Layout of the surface of a CCD (right). [17]

depends on the strip spacing and is given as:

$$\sigma_{\mathrm{MP}} = \frac{p}{\sqrt{12}},$$

where p is the strip pitch. To achieve a x-y resolution two orthogonal layers of strips are used. The smaller is the device, the more reduced is its electronic noise. This gives the pixels an advantage over the strips. Also, the smaller volume results in a better space resolution. The advantage of strips over pixels is in the electronics processing: due to their size, pixels need to be bump-bonded to the front-end electronics, which can prove to be technologically difficult. Strips, on the other hand, are large enough to allow the use of wire-bonding for connection to the front-end electronics.

Semiconductor drift detectors

These detectors use the drift time of charge carriers to determine the position of incoming particle. As can be seen in a scheme in Fig. 2.10a, the n-type bulk is depleted from both surfaces by a series of p^+ electrodes, biased to provide a positive potential gradient along the center axis of the detector. When a particle passes through the depleted area, the holes created drift to the nearest p^+ electrode, whereas the electrons travel to the collection electrode, where the signal is read out. The position is then determined from the time it took the signal charge to drift to the output.

Pixel Detectors

Pixel detectors are finely segmented semiconductor detectors capable of high granularity in detection provided by the pixel size. They are capable of good time and space position resolution. Fig. 2.11 shows a typical pixel cell, a building block of a hybrid pixel detector. The word hybrid denotes that the sensor and electronics are fabricated separately and then assembled together via the so called bump bonding. The ionizing particle crosses a sensor, generating charges along the way that are drifted to the diode where they produce signals. These are then amplified and stored by the electronics.

Apart from hybrid pixel detectors, there are also monolithic pixel detectors; meaning that the detector and readout electronics are integrated in a monolithic structure. However, this method has its drawbacks, such as the basic incompability between the high-resistivity silicon needed for the substantial depletion region of the detector and the lower resistivity silicon used for fabrication of integrated circuits.
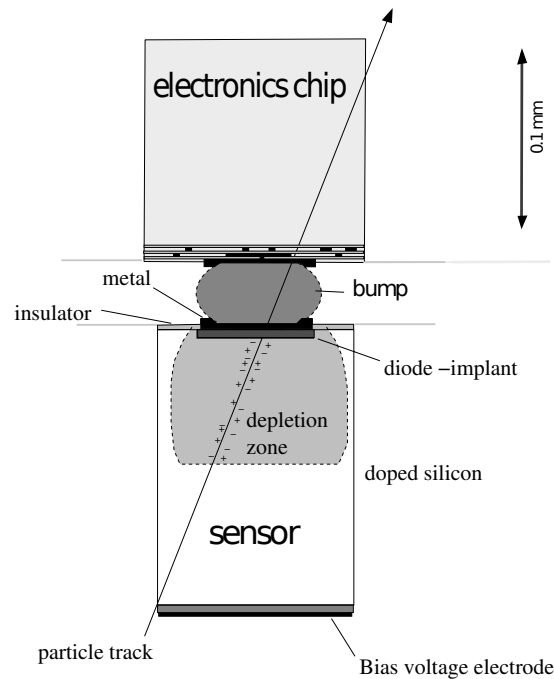
Figure 2.11: Schematic view of one pixel cell. [14]

Charged coupled devices

Charged coupled device (CCD) is nowadays most known for its use in digital cameras. The area of a CCD is built from a large number of small pixels (see Fig. 2.10b for a layout), which are connected and read out together. The signal charge deposited in a pixel is then shifted through neighbouring pixels until it reaches an end. The voltage is set so that every pixel has its own potential well to prevent free electrons from liberating. The advantage of CCDs lies in the simplicity of its serial readout technique and also in its ability to distinguish small charge packets.

2.3.1   The ATLAS pixel detector

The first step in the history of the hybrid pixel detectors was taken in 1984 during the IEEE Nuclear Science Symposium, where a note was presented by Gaalema [26], showing the potential hybridization of detectors via bump-bonding and the concept of a circuit in each pixel. This sparked interest at CERN, a high energy physics laboratory located at the Franco-Swiss border, and a study was performed, whose result was the first pixel circuit with signal processing functions and a binary output. The results of measurement of this chip were presented in 1989. The RD19 collaboration (the LHC detector development collaboration) was interested in pixel detectors because of their capability to handle high track multiplicity, which had been expected at LHC. Thus in 1994, with collaboration of heavy-ion experiment WA97, first pixels were used to collect data. The Delphi experiment at the Large Electron-Positron collider (LEP) practically separated from the RD19 collaboration and developed their own pixel detectors for Vertex Forward Tracker. These detectors were installed in 1997. Further description of the beginnings of the pixel detectors can be found in Ref. [27].

Pixel detectors are currently used in the innermost layer of the ATLAS detector, part of the

Large Hadron Collider (LHC) located in CERN. The aim of the ATLAS is to analyze all particle tracks coming from a collision of protons (or, in some cases, nuclei). This is achieved through an elaborate set of detectors.

The name ATLAS stands for A Toroidal Large ApparatuS with a length of 45 m and 25 m in diameter[2]. Closest to the interaction point is a barrel consisting of pixels (for a closeup of the pixel part see Fig. 2.12). It consists of three layers of radii 5.0, 9.8, and 12.2 cm that are built with 22, 38, and 52 staves respectively. The three barrel layers are made of identical staves inclined with azimuthal angle of 20 degrees. Stave is a building block composed of 13 pixel modules.

In the pixel module (shown in Fig. 2.13) there are 16 front-end (FE) chips and one Module Control Chip (MCC). The FE chips are connected through bump bonding to the sensor. Each chip consists of 2880 pixel covering an active area of 0.74×1.09 cm^2. The MCC serves to connect the front-end chips to the readout system. It has a 45 kbit storage memory dedicated to the event building at the module level. The MCC receives external data and sends its data out through optical fibers. The time resolution of the chips is below 25 ns to satisfy the luminosity requirements at the LHC.

In conclusion, all modules used are equal to simplify the manufacturing process. The sensors are n-doped silicon with n$^+$-pixel implants.

---

[2]As the promotional materials like to point out, this is more than 8 floor high building.
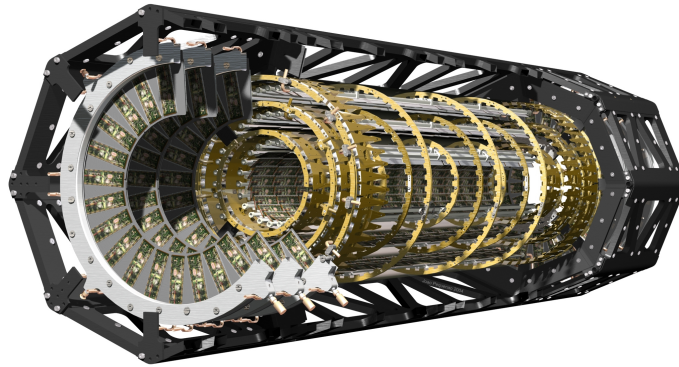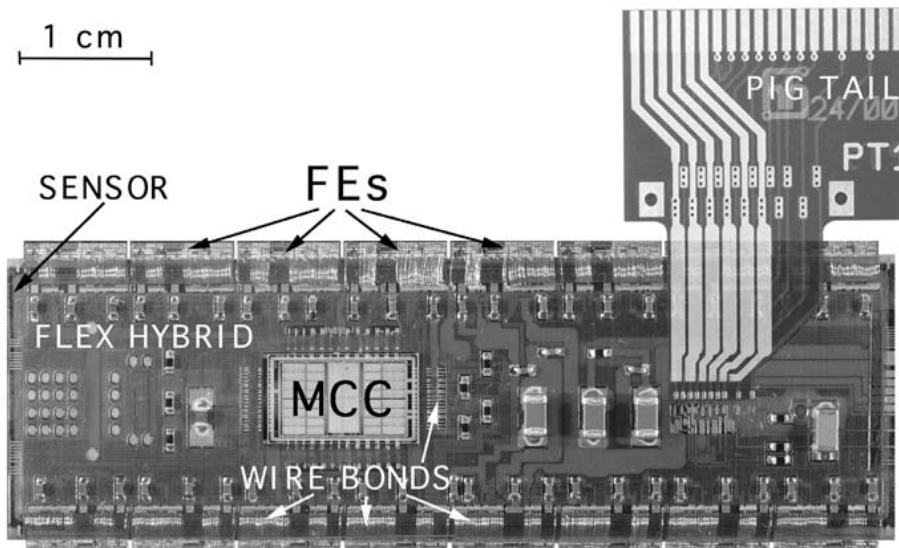
Figure 2.12: The ATLAS Pixel detector. [25]

Figure 2.13: The ATLAS Pixel module. [14]

Radiation hardness

Ionizing radiation invokes changes to the material of the detector called radiation damage. The study of radiation hardness engages in finding and improving the detector resistance to radiation damage and malfunctions caused by radiation. Radiation affects all parts of the semiconductor detector: sensor as well as electronics. All effects are discussed with regard to silicon detectors, which were discussed in previous chapters and were used for the measurement described in the next chapter.

Radiation defects in MOS structures can be divided into two groups: surface and bulk damage. Both types will be further discussed. Radiation measurement was performed with neutrons that cause mainly bulk damage. Radiation effects to the sensor will be described; however, the studied detector comes without sensor.

Interaction of the ionizing radiation with an electron cloud is wanted and used for detection, but interaction with the lattice atoms can cause unrepairable damage to the material. Radiation damage creates both point defects and defect clusters. The cluster model was first proposed by Gossick in 1959 [28], in order to explain a very high minority carrier recombination rate observed after irradiation with heavy charged particles compared to the one observed after gamma or electron irradiation. However, this model is still poorly supported by experimental data, thus not much is known about the exact nature of the defects [19]. Point defects, on the other hand, are intensely studied and classified into appropriate groups.

3.1 Radiation damage in semiconductors

There are two main radiation damage mechanisms:

◆ Displacement damage

◆ Ionization damage

In the first case, the incident radiation displaces silicon atoms from their lattice sites resulting in a defected crystal with changed electronic characteristics. In the latter case, the absorbed ionization energy liberates charge carriers, which then diffuse or drift to other locations where they are trapped, leading to unintended concentrations of charge. Most systems are sensitive to both phenomena.

3.1.1 Displacement damage

Displacement damage is proportional to the non-ionizing energy loss. Since energy loss is a process depending on the mass and energy of the incident quanta, the damage must be specified for a specific particle type and energy.
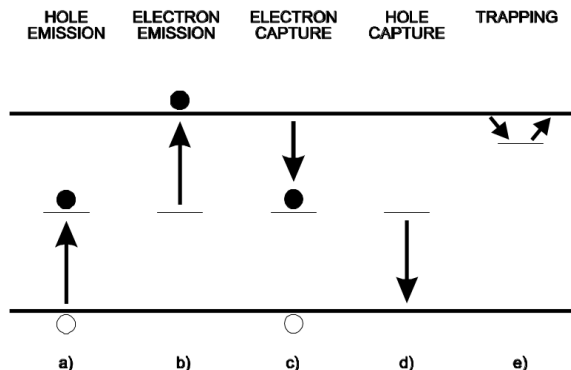
Figure 3.1: Emission and capture processes through intermediate states. [29]

Displacement damage causes formation of mid-gap states, trapping and changes in doping characteristics (donor or acceptor density). The role of the mid-gap states is illustrated in Fig. 3.1. Direct transitions between the conduction and valence bands is highly improbable for Si detectors; however, the presence of intermediate states in the forbidden gap results in a formation of two new processes: emission and capture process (Fig. 3.1a and 3.1b). This easier transition in the depleted region results in an increase of the dark current. Fig. 3.1c and 3.1d show a situation where a defect state captures an electron from the conduction band, which in turn can capture a hole. This process reduces the current flowing in the conduction band and thus reducing detector charge collection efficiency. [29]

Trapping (Fig. 3.1e) is a process in which states close to the band edges capture a charge and release it after a certain time, thus resulting in the reduction of the signal.

Displacement of lattice atoms leads to the creation of new states called interstitials (atoms located between the regular lattice sites) and vacancies (empty lattice site). The defects created can be either stable or unstable. Some defects remain mobile at a room temperature and thus, for example, a moving interstitial can fill the place of a vacancy, which results in a partial annealing, i.e. lessening of the radiation damage. However, under specific conditions a moving defect may form a stable defect. Examples of stable defects created by drift of unstable states are A-center, E-center or divacancy.

An A-center is a vacancy-oxygen complex. Oxygen impurities are always present in the crystal due to the crystal growth process as an inactive interstitial. The complex forms a new acceptor state, thus becoming a trapping center for electrons. An E-center is a vacancy-phosphorus complex that acts as a donor removal. A divacancy, two missing silicon atoms next to each other in the lattice, is an example of a defect that has been formed directly by radiation or may have been present in the crystal from the beginning.

The process of defect complexes formation can be a more-than-one step process, as seen in the examples above. Which defect complexes will form in the lattice depends on many factors, such as temperature, crystal-growing process or space charge region charge.

3.1.1.a   NIEL scaling of bulk damage

The description of the bulk damage is done via the non-ionizing energy loss hypothesis (NIEL). It is based on the observation that the secondary reaction of the knock-on atoms is more or less the same in the detector. Thus, even though the primary interaction differs according to the radiation type and energy, a scaling between different radiation types can be used.

The dependance of the displacement damage cross-section on energy and type of radiation
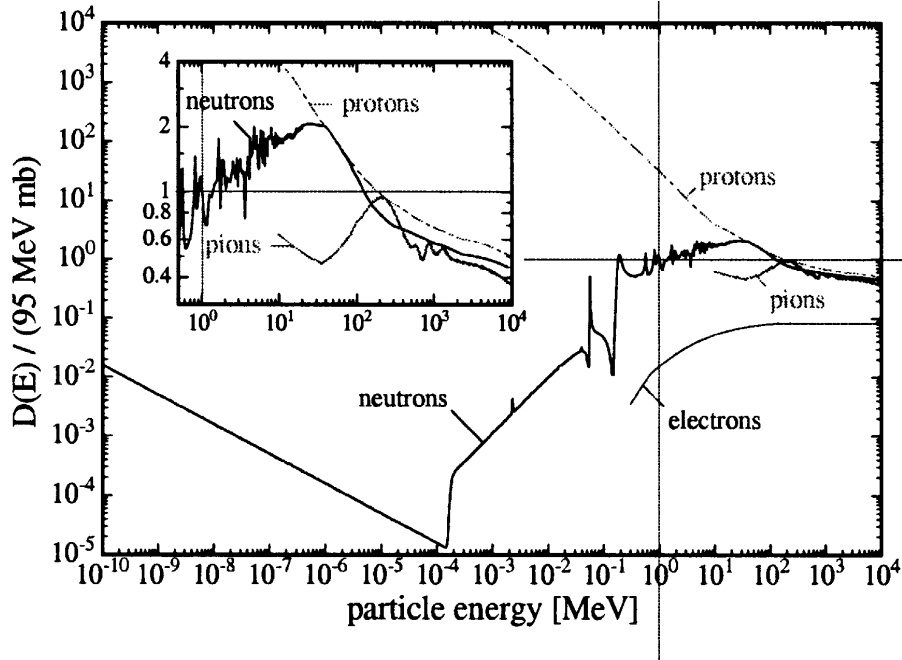
Figure 3.2: Displacement damage function $D(E)$. The insert displays a zoomed part of the figure. [30]

(normalized to 1 MeV neutrons) is shown in Fig. 3.2. It should be noted that not all of the computed values have been experimentally confirmed.

The displacement damage function $D(E)$ is used as an equivalent expression to the NIEL value. The damage efficiency D_{eff} of any particular particle source with an energy distribution of its fluence given by $\Phi(E)$ can be expressed using the appropriate displacement function $D(E)$. The damage efficiency D_{eff} and the total fluence can be related to the displacement damage cross section and the equivalent fluence of 1 MeV neutron producing the same damage. The damage efficiency D_{eff} can thus be defined as:

$$D_{eff} = \int D(E)\Phi(E)\mathrm{d}E = D_{neutron}(1 \text{ MeV}) \cdot \Phi_{eq}, \tag{3.1}$$

with

$$\Phi_{eq} = \kappa\Phi_{tot} = \kappa \int \Phi(E)\mathrm{d}E, \tag{3.2}$$

where κ is the hardness factor characteristic for the source. The displacement damage cross section for 1 MeV neutrons $D_{neutron}(1 \text{ MeV})$ according to the ASTM standards is taken to be 95 MeVmb [31].

Also, opinions against the effectiveness of the NIEL hypothesis have appeared (see Ref. [32] and [33]). Experiments have shown that the NIEL scaling is valid for the damage-induced bulk generation current, but is violated for the change of the effective doping concentration (see Section 3.1.3). This violation is called proton-neutron puzzle and it is a result of the different primary interactions, which for neutrons come from nuclear scattering, whereas for the charged hadrons the Coulomb interaction prevails.

Impurity	Charge state	Energy level	Charge in s.c. region
Phosphorus	P^0 P^+	$E_C - 0.045$	+
Boron	B^- B^0	$E_V + 0.045$	+

Defect	Charge state	Energy level	Charge in s.c. region	T_{ann} [K]
Interstitial	I^- I^0 I^+	$E_C - 0.39$ $E_V + 0.4$	0	$140 - 180$ $540 - 600$ $370 - 420$
Vacancy	$V^=$ V^- V^0 V^+ V^{++}	$E_C - 0.09$ $E_C - 0.4$ $E_V + 0.05$ $E_V + 0.13$	0	≈ 90 150
Divacancy	$V_2^=$ V_2^- V_2^0 V^+	$E_C - 0.23$ $E_C - 0.39$ $E_V + 0.21$	0	≈ 570 ≈ 570 ≈ 140 ≈ 570
A-center	$(V\text{-}O)^-$ $(V\text{-}O)^0$	$E_C - 0.18$	0	≈ 600
E-center	$(V\text{-}P)^-$ $(V\text{-}P)^0$	$E_C - 0.44$	0	≈ 420
Boron interstitial	B_I^- B_I^0 B_I^+	$E_C - 0.45$ $E_C - 0.12$	0	420
Vacancy boron	$(V\text{-}B)^0$ $(V\text{-}O)^+$	$E_V + 0.45$	0	≈ 300

Table 3.1: Characteristics of important defects in silicon. E_C is the conduction band energy and E_V is the valence band energy. [15]

3.1.2 Electrical properties of defect complexes

The defects manifest themself in the change of electrical properties. The main consequences of defects are:

◆ *recombination-generation centers* that result in an increase of a reverse-bias current. The centers are able to capture and emit electrons and holes;

◆ *trapping centers* that lead to a signal reduction. The signal carriers are captured in the centers and emitted with some time delay;

◆ *change of the charge density in the space charge region* which results in the increase of bias voltage needed to make the detector fully sensitive.

In Table 3.1 some known defects in silicon are listed. The impurities added to the silicon lattice can be found in two states: they are either in a neutral defect state (i.e. an occupied state: an additional electron for phosphorus and a hole for boron are bounded with the atom) or a
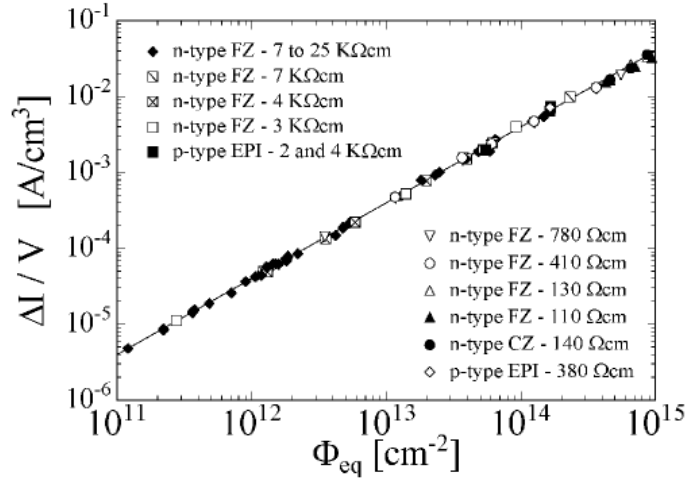
Figure 3.3: Fluence dependence of leakage current for silicon detectors produced by various process technologies from different silicon materials. [19]

positively/negatively charged state for phosphorus/boron respectively. In the latter state, the extra carrier is emitted into the conduction or valence band (the so called empty state). A transition between these two states may occur via electron or hole emission/capture. The third column shows the energy level of the impurities. It also indicates the minimum energy needed for the change of the impurity state. The fourth column of the table shows with what charge is the impurity presented in the space charge (s.c.) region. The last column shows annealing temperatures, i.e. when the temperature of the system rises above the indicated value, the defect is no longer stable.

At the room temperature, the probability for donor/acceptor to be in one of the two states is equal, i.e. it is one half, if the Fermi energy E_F[1] matches the donor energy level E_D. If the Fermi energy differs by few times the thermal energy kT ($kT = 0.025$ eV at room temperature) from the E_D, then one state probability prevails.

Defects can manifest themselves in different charge states. Each charge state corresponds to a particular lattice distortion and a corresponding chemical binding. Every state also carries a specific cross-section value for electron or hole capture describing the probability of the change of states. Similar rules for the occupation probability apply to the defects as they do to impurities. The difference lies in the number of possible states. In reality, a single defect can be in only one charged state at a time. For example, the defect will primarily be in the most negative charge state if the Fermi level is above the highest energy level and vice versa for the most positive charge state. For proper derivation of this statistical problem see Ref. [34].

3.1.2.a   Reverse current

Reverse (also: leakage) current is an omnipresent characteristics of the detector. For an irradiated silicon detector there is a linear dependance of the reverse current I on the active volume V and the equivalent 1 MeV fluence $\Phi_{eq} = \kappa \Phi_{tot}$. For a fully depleted detector it can be written as:

$$I = \alpha \Phi_{eq} V, \tag{3.3}$$

where α is the current-related damage rate. The dependence is shown in Fig. 3.3. It is clearly visible that α is independent of the specific silicon material used for fabrication of the detector and

---

[1]Fermi energy, or Fermi level, is a number when the occupation probability of a (possible) state is one half.
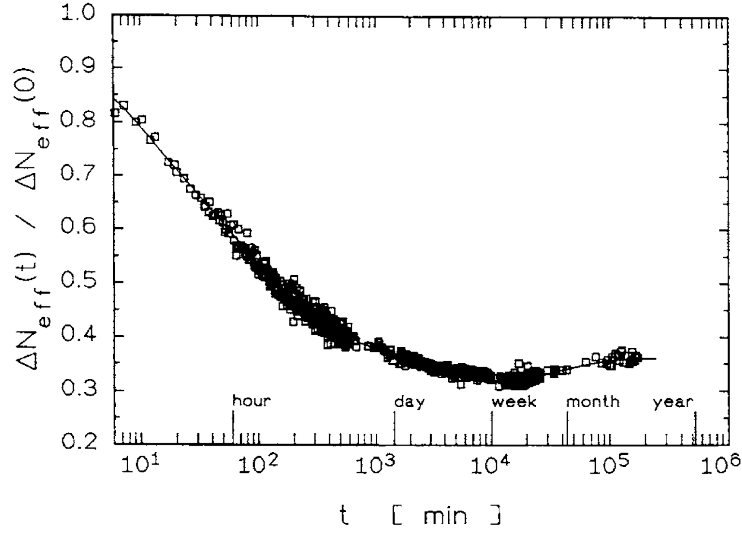
Figure 3.4: Room temperature annealing of radiation-induced change of effective doping. [15]

the process technology used. The abbreviations used in the figure stand for different manufacturing processes; FZ is the float zone method, CZ stands for the Czochralski silicon and EPI is the epitaxial method.

3.1.3   Annealing

Annealing is a process during which the radiation damage to the detector diminishes with time. The most important quantities that effect annealing results are temperature and time since irradiation. As can be seen in the last column of Table 3.1, each defect has its own specific annealing temperature until which it remains stable. The defect may disappear or turn into another stable defect. The radiation-generated effective doping change and the volume-generated current lessen with time, as can be seen in Fig. 3.4. Another phenomenon is visible in the right section of this figure called *reverse annealing.*

Reverse annealing results from the fact that when the old defects anneal, new ones can be formed with worse effects on the detector. There are two different mechanisms proposed to explain this fact: the first one is that with time, the electrically inactive defects transform into active; the latter is that two electrically inactive defects join and form an electrically active with time. Since reverse annealing is an unwanted characteristic, methods how to prevent this from happening were being researched and the result is in its dependency on temperature: below 0 °C, reverse annealing vanishes (moreover, with raising temperature this effect accelerates).

To simulate the long-term annealing effects at the room temperature, the detector may be left to anneal at a higher temperature for a shorter time. For example, 80 minutes at annealing temperature $T = 60$ °C are equivalent to about 10 days at room temperature.

In mathematical terms, annealing is a process, which changes the effective doping concentration $N_{extiteff}$ of the detector bulk. $N_{extiteff}$ is also called the effective impurity concentration and is defined as follows:

$$N_{extiteff} = |N_d - N_a|,\tag{3.4}$$

where N_d and N_a are the positively charged donor and negatively charged acceptor concentration.

Beneficial annealing	$g_A = (1.92 \pm 0.05) \cdot 10^{-2}$ cm^{-1}
$E_a = (1.09 \pm 0.09)$eV $\Rightarrow$	$\tau_a(60\ °\text{C}) = 20$ min, $\tau_a(20\ °\text{C}) = 2$ days
Reverse annealing	$g_Y = (5.16 \pm 0.09) \cdot 10^{-2}$ cm^{-1}
$E_a = (1.31 \pm 0.04)$eV $\Rightarrow$	$\tau_a(60\ °\text{C}) = 1000$ min, $\tau_a(20\ °\text{C}) = 350$ days
Stable acceptors	$g_C = (1.49 \pm 0.03) \cdot 10^{-2}$ cm^{-1}
Partial donor removal	$N_{C0} = (1.92 \pm 0.05) \cdot 10^{-2}$ cm^{-1}

Table 3.2: Parameters of the Hamburg model as fitted to the experimental data. [19, 37]

The effective doping concentration can be calculated with the use of the depletion voltage V_d:

$$N_{extiteff} = \frac{2\varepsilon\varepsilon_0}{ed^2}V_d, \tag{3.5}$$

where $\varepsilon\varepsilon_0$ is the permittivity in silicon, e the elementary charge and d the detector thickness. During irradiation the study of the change of the effective doping concentration $\Delta N_{extiteff}$ is performed. $\Delta N_{extiteff}$ is defined as the change between the initial doping concentration of the base material and its value after irradiation and can be parametrised as:

$$\Delta N_{extiteff} = N_A(\Phi_{eq}, t(T)) + N_C(\Phi) + N_Y(\Phi_{eq}, t(T)). \tag{3.6}$$

Concentration change $\Delta N_{extiteff}$ is defined as a function of the equivalent fluence Φ_{eq} and the annealing time t at the temperature T. It consists of three components: a short-term beneficial annealing N_A, a stable damage part N_C and a reverse annealing component N_Y. The three components can be further described as:

$$N_A = \Phi_{eq} \times \sum_i g_{Ai} \cdot \exp\left(-t/\tau_i\right), \tag{3.7}$$

$$N_Y = N_{Y,\infty}\left(1 - \frac{1}{1 + t/\tau_y}\right), \tag{3.8}$$

$$N_C = N_{C0}\left(1 - \exp\left(-c \cdot \Phi_{eq}\right)\right) + g_C\Phi_{eq}. \tag{3.9}$$

Both time constants τ_i and τ_Y are strongly dependant on the temperature; g_i are additional parameters of the model. The short term annealing N_A is described as a first order decay of acceptors introduced proportional to Φ_{eq} during irradiation, where g_C is the generation rate responsible for the formation of stable acceptors. Stable damage N_C is not dependant on annealing and it consists of an "incomplete donor removal" and stable acceptors. The reverse annealing component N_Y is described as a second order parameterisation, where $N_{Y,\infty} = g_Y\Phi_{eq}$.

The described parametrisation of annealing is called Hamburg model [35, 36]. Parametrisation of the model applied to the measured data can be seen in Fig. 3.5. Table 3.2 shows the various values as extracted from a fit to experimental data for a high-resistivity n-type FZ silicon. E_a is the activation energy for the given temperature dependance.

3.1.4 Ionization damage

Ionization damage is proportional to the absorbed energy, independent of the type of radiation. However, the resulting effects depend on the rate of irradiation, the applied voltages and their time variation, the temperature, and the time variation of the radiation itself. Holes are more affected by the ionization damage, because of their lower mobility and complicated hopping mechanism in the crystal that makes it easier to be captured in traps and thus creating defects. Since the
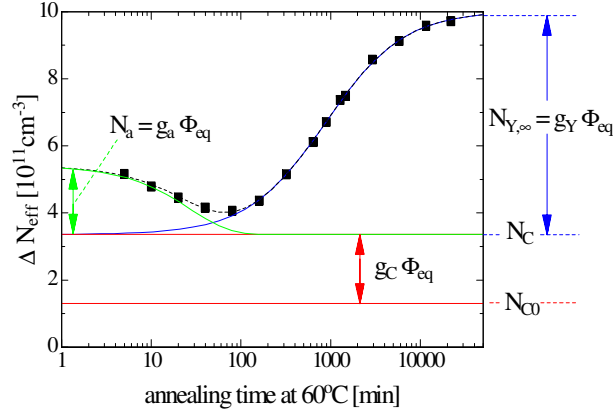
Figure 3.5: Different components of the $\Delta N_{extiteff}$ annealing as parameterised by the Hamburg model applied to data. The sample was irradiated with a neutron fluence of 1.4×10^{13} cm^{-2} and annealed at a temperature of 60 °C. [30]

charge liberated depends on the absorber material, the ionizing dose must be referred to a specific absorber, e.g. 1 Gy(Si).

Ionization damage can cause the formation of a parasitic field. The ionization effects are determined by various attributes: the oxide-silicon interface trapped charge, the mobility of the trapped charge and the time and voltage dependence of charge states. [29]

3.1.4.a   Surface damage

Ionization causes damage in surface regions of the detector. In the case of silicon detector this involves not only the surface passivation of the detector, but also at the interfaces such as Si/SiO$_2$. Surface damage can be annealed at temperatures above 150 °C.

Without an electric field, electrons and holes recombine quickly. However, when the electric field is present, electrons are quickly swept away and holes transfer slowly to the Si/SiO$_2$ interface, where they are trapped. This causes an increase of the oxide charge and creation of the surface generation centers.[38]

3.2   Radiation damage in silicon detectors

Silicon particle detectors can be simply described as a sensor bulk and the adjacent readout electronics. Both these parts suffer from radiation damage. Radiation damage of the sensor manifests itself by an increase of the leakage current and by increasing the full depletion voltage. To understand why electronics undergoes radiation damage it is important to note that the basic building block of electronics today is a MOSFET transistor, which is again a semiconductor device. Therefore, during the design of the detector it is important to focus on both parts from the point of radiation damage.

One of the radiation damage mechanisms in silicon particle detectors is caused by displacing a primary knock on atom from its lattice resulting into a so-called Frenkel pair: a silicon interstitial and a left over vacancy. Displacement energy E_d is the energy at which the displacement probability is roughly equal to one half; for silicon $E_d = 25$ eV. Displacement energy is a special case of a recoil energy E_R of the atom: if $E_R < E_d$ it will mostly lead to lattice vibrations only and if $E_R > E_d$ the

Radiation	Interaction	T_{max} [eV]	T_{avg} [eV]
Electrons	Coulomb scattering	155	46
Protons	Coulomb and nuclear scattering	133 700	210
Neutrons	Elastic nuclear scattering	133 900	50 000

Table 3.3: Characteristics of interaction with silicon and of primary knock-on atoms. The radiation energy is 1 MeV. T_{max} is the maximum kinematically possible recoil energy and T_{avg} is the mean recoil energy. [15]
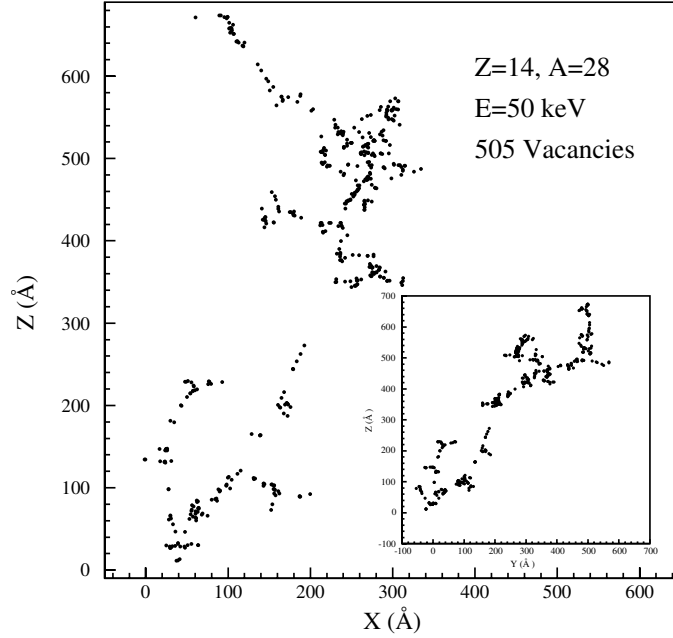

Figure 3.6: Simulation of a spatial distribution of vacancies created by a 50 keV Si-ion in silicon. The inset shows the transverse projection of the same event. [32]

silicon atom will create a point defect, an additional vacancy-interstitial pair. If the recoil energy is above 2 keV, a defect cluster will be formed. A list of energies of different radiation sources is shown in Table 3.3, showing that under the conditions described in the legend of the table, electrons do not form clusters, whereas protons and neutrons may. Since both interstitials and vacancies are very mobile, a large part of Frenkel pairs recombines at the room temperature and no damage remains.

Neutrons, the irradiation source used in the measurement, need a kinetic energy of ≈ 185 eV for the production of a Frenkel pair and more than ≈ 35 keV to produce a cluster. In Fig. 3.7, a simulation of the lattice damage caused by a recoil-atom with the recoil energy $E_R = 50$ keV is shown. The energy value of the PKA is chosen as the approximate energy that is transferred to the atom if the ionizing particle is a 1 MeV neutron. The generation of clusters is clearly visible in the Figure.

Another mechanism contributing to the radiation damage is ionization damage. This damage is caused by holes trapped in the SiO_2 that act as a space charge. However, for silicon particle detectors this mechanism has smaller effect (10^{-3} compared to the neutron of the same energy [39]).
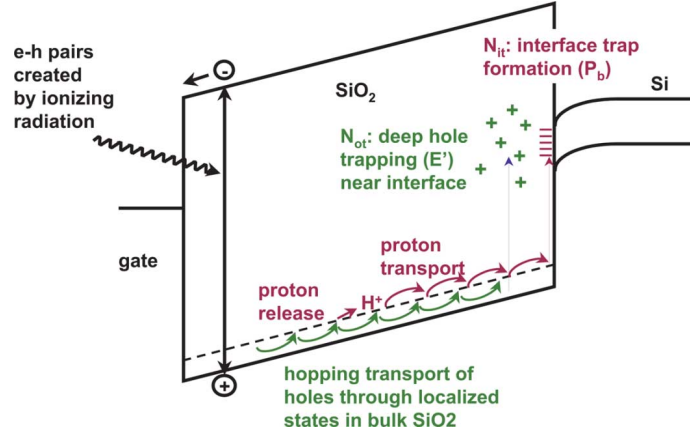
43

Figure 3.7: Band diagram of an MOS capacitator with a positive gate bias. Illustrated are the main processes for radiation-induced charge generation. [39]

3.2.1 Radiation effects in MOS oxides

Radiation effects in MOS oxides come mainly from two sources: oxide-trap and interface-trap charge buildup. A band diagram showing the main processes for radiation-induced charge generation is shown in Fig. 3.7.

As mentioned before, holes move through the oxide at a slower rate than electrons. In the presence of an electric field, holes can transport to either the gate/SiO_2 (negatively applied bias) or the Si/SiO_2 interface (positively applied gate bias). Due to their charge, holes create a distortion of the local potential field of the SiO_2 lattice, effectively trapping themselves at the localized state. A combination of the charged carrier (hole) and its strain field is known as a polaron [40]. The movement of holes in the SiO_2 lattice is then called "polaron hopping". Polarons increase the effective mass of the holes and decrease their mobility. [39]

Radiation also leads to the formation of interface traps at the Si/SiO_2 surface. These traps exist within the silicon band gap at the interface and result in the threshold voltage shifts. For a p-channel transistor, interface traps are mainly positive, causing negative-threshold voltage, whereas for a n-channel transistor the opposite signs apply. At midgap, interface-trap charge is approximately neutral. This damage takes longer time to build up than oxide-trap damage and, unlike oxide-trap charge, does not anneal at the room temperature, but at higher temperatures.

The total threshold-voltage shift caused by the oxides irradiation is given as the sum of the threshold-voltage shifts due to oxide-trap and interface-trap charge:

$$\Delta V_{th} = \Delta V_{ot} + \Delta V_{it}. \tag{3.10}$$

ΔV_{ot} and ΔV_{it} can be determined from:

$$\Delta V_{ot,it} = \frac{-1}{C_{ox}d} \int_0^d \rho_{ot,it}(x)x \ \mathrm{d}x, \tag{3.11}$$

where d is the oxide thickness, C_{ox} is its capacitance and $\rho_{ot,it}(x)$ is the charge distribution of radiation-induced oxide-trapped or interface-trap charge. For positive charge, the threshold-voltage shift is negative; conversely, for a negative charge, the threshold-voltage shift is positive. Thus, for devices where oxide-trap charge dominates, the threshold-voltage shift will be predominantly negative. [39]
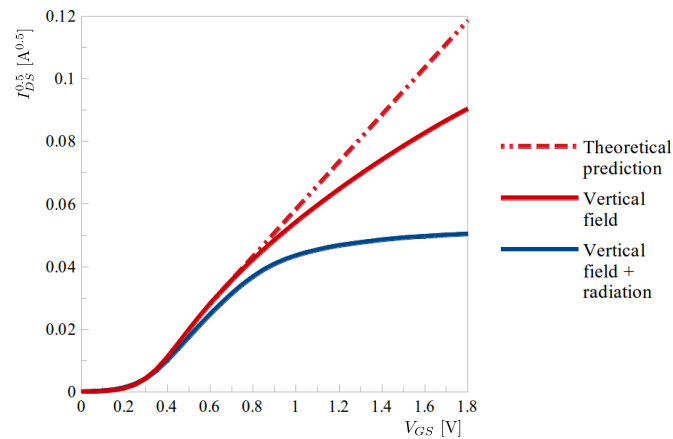
Figure 3.8: The vertical field mobility degradation.

3.2.2 Vertical field mobility degradation

Radiation defects created in the MOS oxides lead to the vertical field mobility degradation in MOS transistors. The degradation is observed as a deviation from the linear dependence of the $I_{ds}^{0.5}$-V_g characteristic of the MOSFETs, which is theoratically predicted as a square root of Eq. 2.12. This effect is observable during operation at high gate-source voltages. Since the oxide cannot be processed without impurities, some local charge distortions are always present. In the presence of high electric field, the charge carriers are attracted to the insulation layer and their movement can be disturbed by a rebounding from the oxide instead of an undisrupted passage through the channel. This results in a decline of observed $I_{ds}^{0.5}$-V_g characteristics in the high voltage region.

In case the transistor has been irradiated, more deffects are created in the oxide and the degradation effect is more profound. The vertical field mobility degradation effect for unirradiated and irradiated data and the deviation from theoretical value is shown in Fig. 3.8.

Experimental measurements

This chapter describes the measurement of radiation effects and their analysis performed by the author of this thesis. The measurement was performed on test structures integrated on a PH32 chip, which was developed under the project TE01020069. The tested chip has been irradiated by a combined neutron and gamma field at the nuclear research reactor LVR-15 of the Research Centre Rez Ltd in Rez near Prague.

4.1 Irradiation setup

Samples were irradiated by a combined neutron and gamma field produced in a core of nuclear reactor. They were shielded by a 0.5 mm thick Cadmium shield. The radiative capture effect in cadmium shields the sample from thermal neutrons (as can be seen in Fig. 4.1) but it lets through epithermal neutrons which can still be captured in silicon and cause transmutation, however, at a rate much smaller than thermal neutrons. The neutron capture cross-sections of ^{112}Cd ($\approx 24\%$ of cadmium) and ^{28}Si ($\approx 92\%$ of silicon) are shown in Fig. 4.1.

Chips were irradiated by a mixture of neutron and gamma field, however, with the current setup at the reactor it is non-trivial to separate effects of those fields and even define their individual contributions. The MC simulated neutron and photon fluxes are shown in Fig. 4.2; they were computed using the MCNPX framework (version 2.7.0) with a ENDF/B-VII.0 library [42, 43]. The
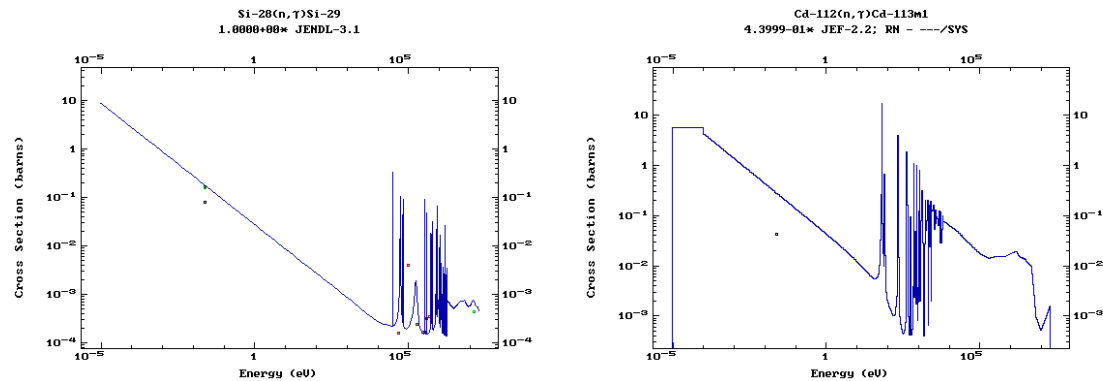

Figure 4.1: The neutron cross-sections of ^{28}Si (left) and ^{112}Cd (right). Cross=sections for other isotopes can be found at [41]
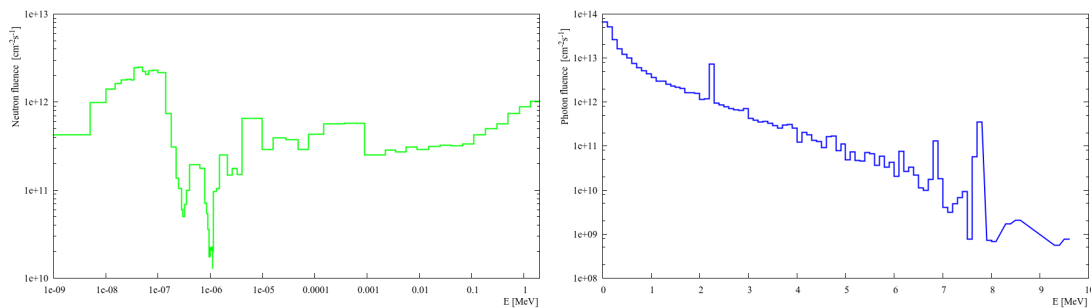
Figure 4.2: The MCNPX simulated energy spectrum of neutrons (left) and photons (right) at the research reactor at Rez.

simulated environment was the core of the reactor with an empty capsule with a Cd shield in which the irradiated sample was placed. Peak of epithermal neutrons is clearly visible at around 100 meV. Only neutrons with energies larger than 185 eV can cause displacement damage to Si crystal lattice. The photon spectrum shows the typical reactor spectrum; photons from radiative capture in cadmium are insignificant compared to the reactor photon flux.

4.1.1 Radiation source

The reactor LVR-15 is a light water tank-type research reactor with a small core placed in a stainless steel vessel under a shielding cover. The maximal power output is 10 MW. Maximum achievable thermal neutron flux is $10^{14}\text{n} \cdot \text{cm}^{-2}\text{s}^{-1}$. The fuel used in the reactor is 19.75% enriched ^{235}U. The irradiation tube is placed behind the reflector. The configuration of the core during the irradiation is shown in Fig. A.1. [44]

4.1.2 PH chips

PH32 chip is designed to read out electrical signals from different (in size and/or geometry) sensing elements; it is capable of reading out 32 detector channels. The layout of the integrated circuit PH32 is shown in Fig. 4.3. The chip was fabricated using commercial 150 nm CMOS technology. The PH32 chip is composed of two parts: the 32 readout channels and the accompanying processing part. Each channel is composed of the analog part (signal amplification), which outputs an electrical signal which is then compared with a threshold value. If the signal amplitude is in the accepted range, a discrete digital value (0 or 1) is passed onto the second part of each channel, which consists of a digital processing elements. The constitution of the analog and digital part of the PH32 chips is different; e.g. the digital part consist of many small transistors in contrast to the analog part which contains a small number of large transistors.

Eight test structures were manufactured onto these chips in order to study their properties under irradiation. The test structures consist of 8 different versions of MOSFET transistors, The transistors have a common gate and a common source. The test structures consist of different types of transistors and insulation from the bulk material. The first four (TS0 – TS3) are of NMOS type and the latter are of PMOS type. They also vary in width and length of the MOSFET channel and whether they are placed in an isolation layer called Deep N-Well (DNW). The complete list of TS properties is shown in Table 4.1 and their detailed view is shown in Fig. 4.4. W/L ratios of 10 and 0.1 were selected to study effects on narrow and long channels. Wide transistors have multiple fingers and therefore multiple leakage paths can be created during irradiation. Every TS consists
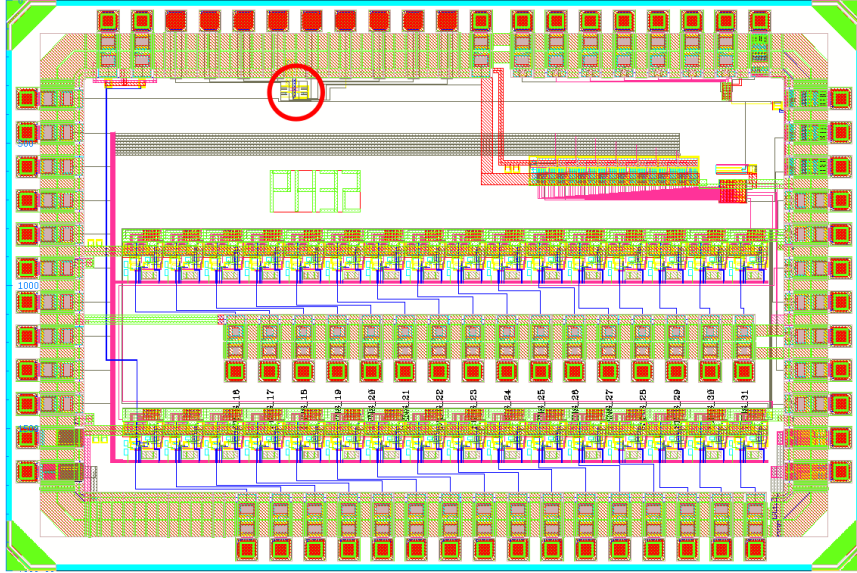
47

Figure 4.3: Layout of the PH32 chip. The position of the test structures on the chip is marked by a red circle. In the bottom half of the figure, the 32 readout channels are visible.

Name	Transistor	Width [μm]	Length [μm]	Number of fingers
TS0	NMOS	6	0.6	4
TS1	NMOS	0.6	6	1
TS2	NMOS-DNW	6	0.6	4
TS3	NMOS-DNW	0.6	6	1
TS4	PMOS	6	0.6	4
TS5	PMOS	0.6	6	1
TS6	PMOS-DNW	6	0.6	4
TS7	PMOS-DNW	0.6	6	1

Table 4.1: Test structures and their properties.

of 10 identical transistors connected in parallel to increase the sensitivity of the measurement to the radiation effects.

Each test structure was measured individually during the measurement. Two Keithley 237 source measurement units were used as the source of the gate and drain-source voltage. For the I-V measurements, the drain-source current was measured for a given voltage, which varied from 0 V to 1.8 V in 50 mV steps.

4.1.3 Irradiation scheme

In preparation for irradiation, the chips were placed in a test tube and then placed in a Cd capsule. Due to its high cross-section for slow neutron capture, most of the thermal neutrons were absorbed in the Cd and did not influence the measured chips.

The irradiated capsules were then transported from the reactor's core into the hot cells that are located in the reactor building, below floor level of the reactor hall. The chips were there extracted
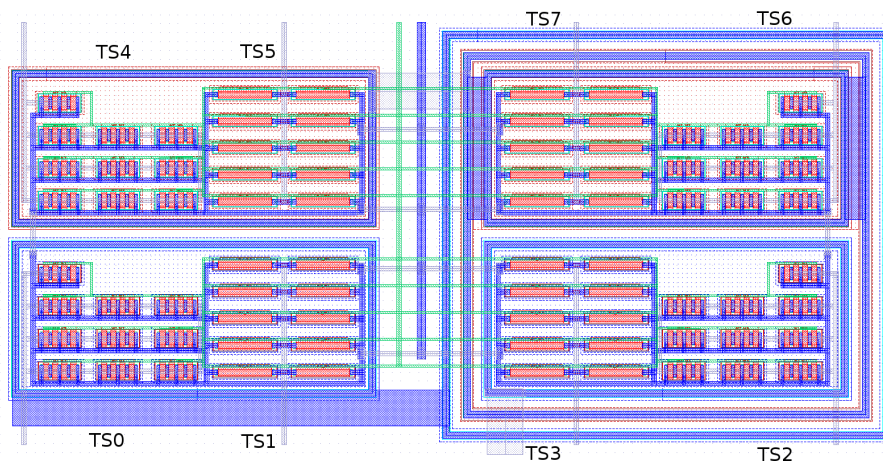
Figure 4.4: A detailed view of the test structures. The test structures number 0, 1, 4, and 5 are shown in the left part of the figure. The remaining test structures 2, 3, 6, 7 are placed in a deep n-well (blue rectangle) on the right.
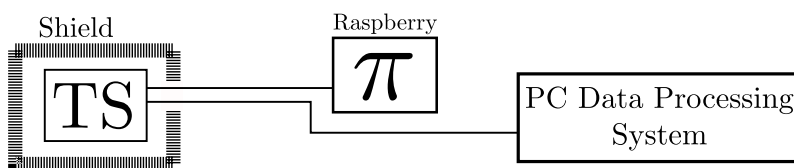

Figure 4.5: Simplified experimental setup. Only shown are the readout devices; source measurement units are not shown.

from their capsules and shielding and placed into the measurement setup. If needed, they were left to cool down in the hot cells.

The measurement setup is shown schematically in Fig. 4.5. The setup was placed next to the hot cells, in the service room. The chips on which were the measured test structures (TS) fabricated were connected to Raspberry Pi, which serviced the digital configuration of the chip itself. The information obtained via this way used in the performed analysis were the analog and digital current of the chips. The other connected device was the PC, which recorded the voltage and current output of the test structures.

4.2   Measurement results

The chips were inserted into the reactor, each sample with increasing time of irradiation. PH32-D was irradiated on April 1 2014. The following day PH32-E was irradiated and finally on April 3 the last chip, PH32-F, was irradiated. The irradiation times and total absorbed dose of the chips in the reactor are shown in Table 4.2. The recorded fluence is that of the neutrons in an energy range $0.1 - 20$ MeV, lower energy neutrons were shielded. The first measurement after irradiation was performed with one hour delay for the PH32-D chip; the remaining two chips were left to cool down for one day after irradiation before the first post-irradiation measurement.

The test structure No. 6 of the PH32-F chip was excluded from all the presented results because it was not possible to properly measure its characteristics.

Name	Duration of irradiation [s]	Measured fluence $[10^{14} \cdot \text{n/cm}^{-2}]$
PH32-D	60	9.3
PH32-E	270	30.2
PH32-F	900	81.8

Table 4.2: Measured samples, duration of their irradiation and measured neutron fluences.

4.2.1 MOSFET IV characteristics

Current-voltage characteristics of the transistors in the test structures of all the chips were measured. Even though the irradiation lengths varied, some common tendencies can be found.

Measured I-V characteristics of any given test structure were shifted by irradiation.The radiation damage to the transistor was found to be greater in a PMOS than in a NMOS transistors. The lowering of the drain-source current was $\approx 1\%$ for the NMOS transistors and $\approx 10\%$ for the PMOS transistors. This could indicate that the radiation damage in a PMOS structure was larger than in a NMOS structure. However, such results contradict the ionization-damage hypothesis, and more likely point to another underlying effect. Discussion of observation of such an effect is in the next section.

Annealing behavior of the test structures is observed. The data show a tendency to return to the preirradiation value of the current-voltage characteristics with increasing time.

The measured I-V characteristics of the test structures of the PH32-E chip are shown as an example in Fig. 4.8.

4.2.2 Threshold voltage

Threshold voltage value has been extracted from the measured data. This variable was defined in Eq. 2.12 The transition from the weak to strong inversion is gradual, and so it is difficult to obtain specific threshold value directly from the I_{ds}-V_g characteristics, but it has to be obtained indirectly from the data. This resulted in the development of many extraction methods, which are presented in Section 3.1 of Ref. [45].

The extraction of the threshold voltage value performed in this work was based on the *linear extrapolation* method from Ref. [45]. The principle of this method is shown in Fig. 4.7. The figure shows the voltage threshold extrapolated value of a PH32-D chip and its TS0. An inflexion point is found on the $I_{ds}^{0.5}$-V_g curve (its position is highlighted in green), around which a linear fit is constructed from four neighbouring datapoints. The data for the gate voltage are taken so that the drain-source voltage was at the same value, schematicaly written $V_{gs} = V_{ds}$. This fit in the linear region of the curve is then extrapolated to the axis intercept point $I_{ds} = 0$. The inflexion point value was obtained through double numerical differentiation. The intercept point was then found with the results of the linear fit of the surrounding points; for a fit given as $I_d = a \cdot V_g + b$, the intercept point is given as $V_g = -a/b$.

A shift of this value is expected after irradiation due to the radiation-induced trapped field oxide charge and trapped interface charge . The results of this method with their standard deviations are shown in Fig. 4.8. The pre-irradiation values of the threshold voltage of the transistors were found to be for TS0 and TS2 around 280 mV, for TS1 and TS3 around 210 mV, for TS4 and TS6 around -455 mV and finally for TS5 and TS7 around -470 mV. A shift is visible in the extrapolated value of threshold voltage after irradiation. The largest percentual shift was observed for the TS1 and TS3 structures for the NMOS structures. The PMOS transistors seemed to all undergo the same percentual shift. The NMOS transistors experienced shift of the threshold voltage of average 5 mV, whereas the PMOS transistors experienced shift of the order of tens of mV. Dependence
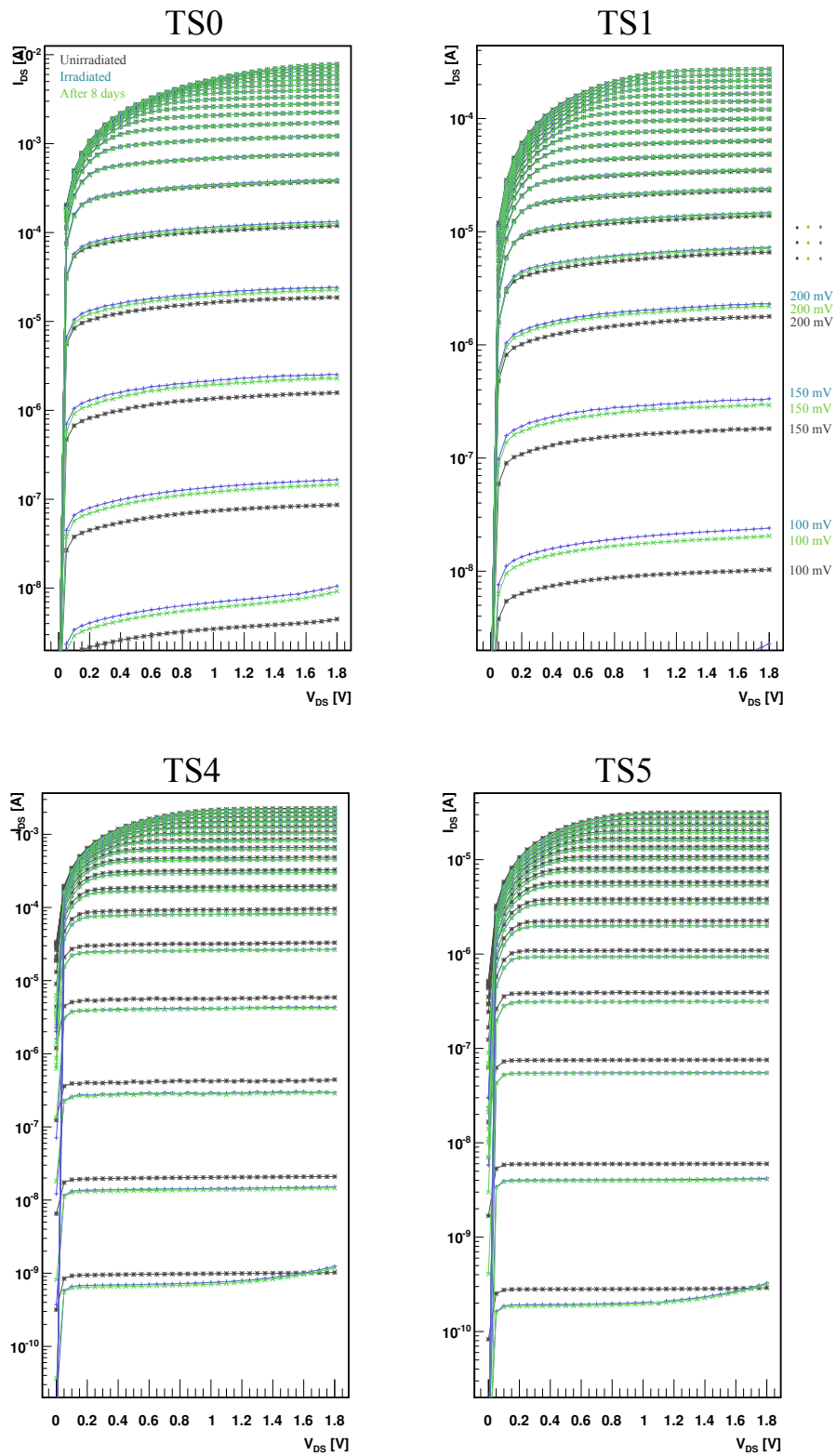
Figure 4.6: The MOSFET IV-characteristics of the PH32-E chip before and after irradiation. The parameter of the characteristics is the gate voltage which was adjusted in 50 mV steps.
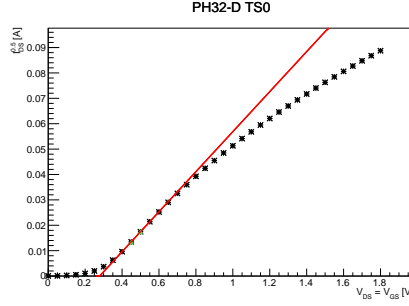
Figure 4.7: The principle of linear extrapolation method. An inflexion point is found on the plotted curve (shown in green points) and an intercept with the x-axis of a linar fit around the inflexion point is taken as a threshold voltage V_{TH}.

of the threshold voltage on the placement of the TS in the DNW was not observed. Once left to anneal at room temperature, both of the values started to return to their preirradiation values. The NMOS transistors experienced lowering of their threshold voltage, suggesting that they reach strong inversion faster after irradiation. The PMOS transistors experienced a rise in their threshold voltages. The shifts can be explained as a consequence of the ionizing radiation, which induced positive charge in the insulating layer of SiO_2. The results were in accordance with the results of the radiation study [46].

4.2.3   Mobility degradation

Vertical field mobility degradation effect has already been described in Section 3.2.2. There exists also a horizontal field effects which states that for large electrical fields between drain and source, the mobility of the charge carriers reaches saturation. However, the horizontal field effect was not observed in the measured data.

Mobility degradation, which is proportional to the increased channel resistance, was observed in the PH32-F chip. The effect was not studied for other measured chips, since for the lower fluences the observed degradation was not as pronounced. The shift of their $I_{ds}^{0.5}$-V_g characteristics, which is observed with these chips, can be explained as a shift of the threshold value. In the case of the PH32-F chip, the difference is substantial enough to try to differentiate the underlying effects. The prediction for the vertical field mobility degradation is in correspondance with the measured data. In fact, the illustrational image used in the Section 3.2.2 shows plotted dependence of the TS2 of the PH32-F chip.

Mobility degradation reduces the maximum drain current. The degradation of the maximum current has been measured and is summarized in Table 4.3, where I_{max} is the maximal preirradiation value, I_{rad} is the maximal post-irradiation value and I_{ann} is the maximum value after annealing. The transistor current reaches its maximum value when gate voltage is 1.8 V for the NMOS and 0 V for the PMOS transistors.

4.2.4   Current consumption

The different electronical architecture of the analog and digital part of the PH32 chips translates into the different current consumption, which is studied in this section. The change in current consumption value due to an irradiation is an important characteristic for the potential detector application of the chip.
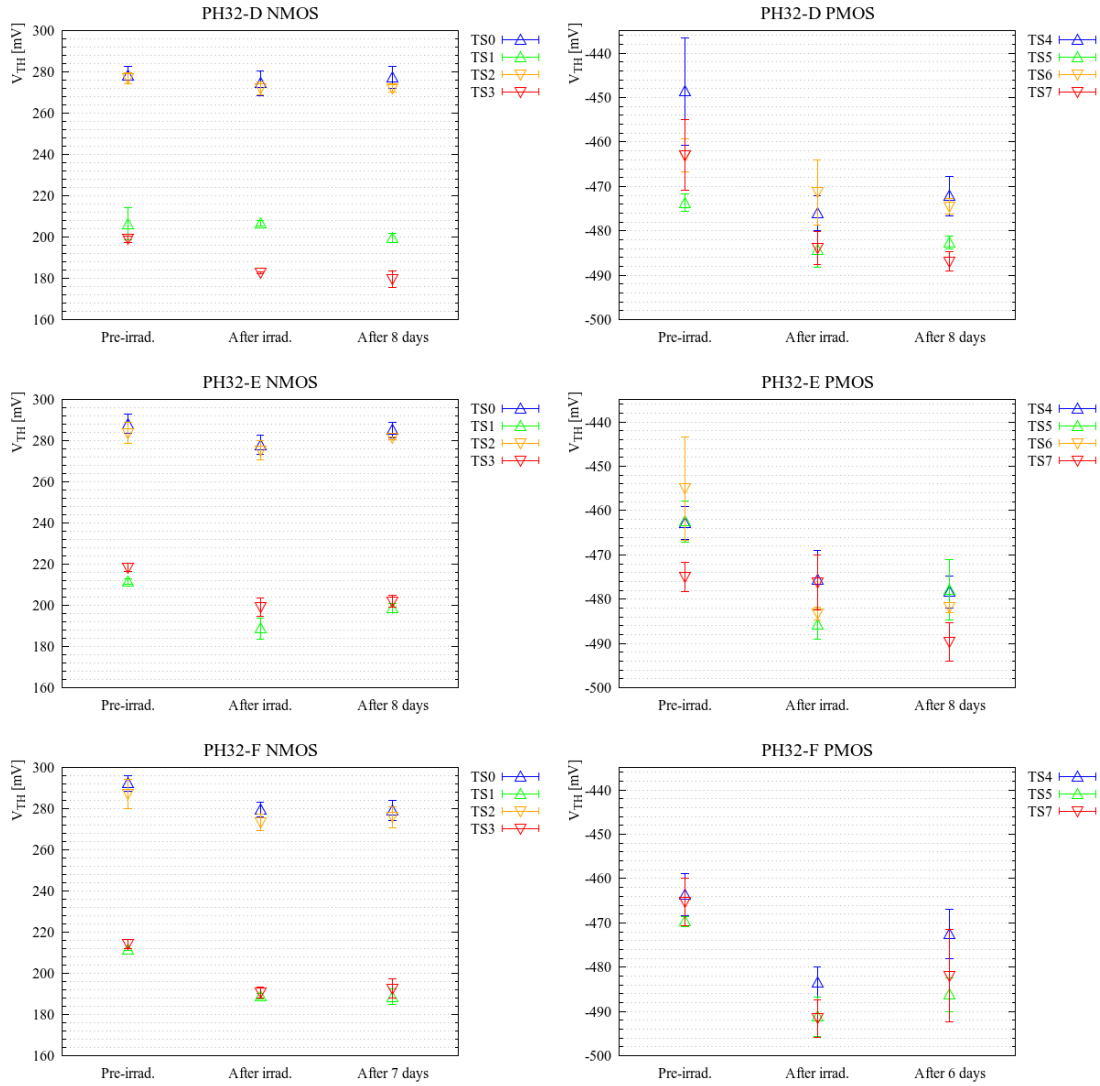
Figure 4.8: The threshold voltage shift of the measured MOSFETs on samples. NMOS test structures on the left, PMOS structures on the right.

	I_{max} [mA]	I_{rad}/I_{max} [%]	I_{ann}/I_{max} [%]
TS0	7.809	99.36	99.48
TS1	0.277	98.77	98.92
TS2	8.199	99.39	99.29
TS3	0.297	98.42	98.52
TS4	-2.289	93.47	95.52
TS5	-0.032	92.52	93.41
TS7	-0.033	91.48	92.04

Table 4.3: The mobility degradation of the PH32-F chip studied with currents.

A shift in both the analog and digital current consumption was observed. The results can be seen in Fig. 4.9, where the current dependency on time in days is shown. The first datapoints at time $t = -1$ day stand for the preirradiation measurement. The preirradiation measurements of PH32 chips were performed at the measurement setup. Since the properties of silicon depend on temperature, it should be noted that the temperature near the measurement setup was fluctutating between $18 - 20$ °C.

The currents for the different PH32 chips follow the same tendency, except for the PH32-F chip, whose preirradiation analog value is six times smaller than was expected and the preirradiation digital value is higher than the post-irradiation ones, which is a discrepancy with the other measured chips. This happened probably due to the cold contact on the chip during the measurement. These values should not be taken into account during analysis of the currents. It can be seen from the results, that for the PH32 chips both analog and digital values of the currents rose after irradiation. This observation reflects the fact that as the device undertakes radiation damage, a larger current is needed to operate the device at the same conditions as were the preirradiation ones and to overcome the effects of radiation damage.

The figures also show that even though the chips were left to anneal for up to 8 days, the current values never returned to their preirradiation state. No direct sign of annealing was measured with certainty because of the fluctuations of the values of the measured currents.
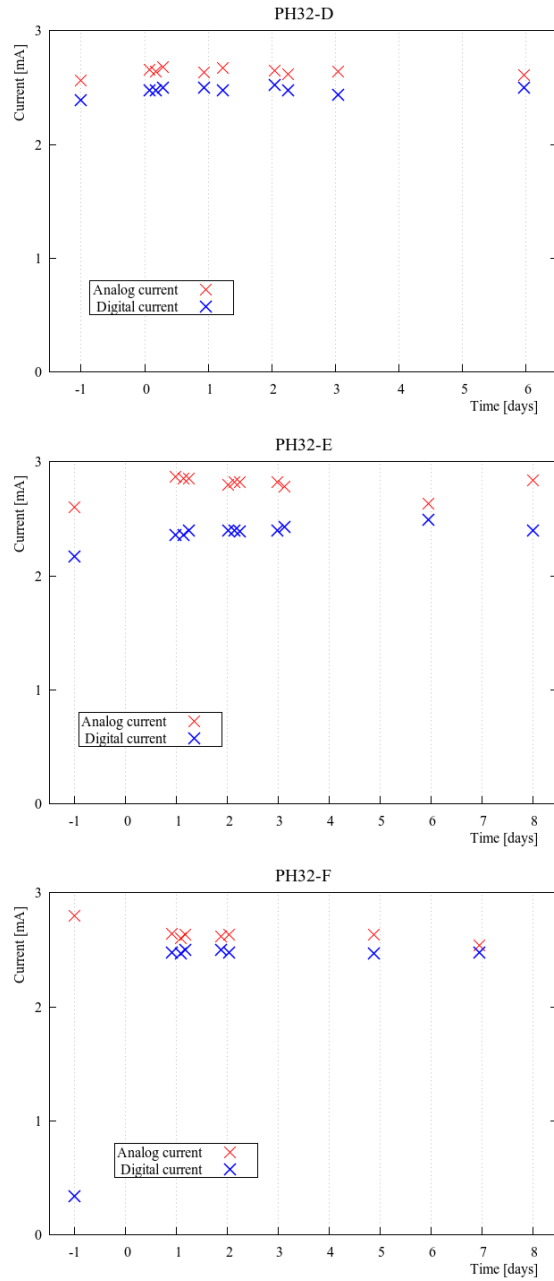
Figure 4.9: Measured analog and digital currents of the studied chips. Data at the stamp -1 represent the preirradiation value.

Conclusions

The first three chapters of this thesis give a short presentation of several topics. First, the way particles interact and their classification is given. Next, semiconductor material properties and semiconductor detectors are presented. The third chapter consists of description of radiation damage. All these chapters were written to give a proper background for the last chapter, that presents the results of a measurement performed with semiconductor devices concerning radiation hardness.

The studied test structures are a part of the PH32 chip, a chip designed to readout 32 detector channels. The results of the measurement of the test structures measured in a neutron nuclear reactor can be concluded as follows. Because of the irradiation, the current-voltage characteristics of the test structures were changed. It appears that the PMOS transistors were damaged more by the radiation than the NMOS transistors. The structures were left to anneal for up to 8 days and an improvement of the current-voltage characteristics was observed.

Another measured characteristics of the test structures was the threshold voltage. A shift was observed in the extracted values of the threshold voltage; a rise for PMOS transistors (tens of mV) and a fall for NMOS transistors (around 5 mV).

Mobility degradation was observed for the PH32-F chip and it was explained as a direct result of two effects: the vertical field mobility degradation effect and the radiation induced mobility degradation effect. For the combination of these effects, the mobility degradation of charge carriers reduces the maximum transistor current of NMOS devices by $\approx 1\%$ and of PMOS devices by $\approx 7\%$.

In conlusion, results in this work show that the overall changes of the properties of the chip and its test structures were only slightly affected by the radiation. The chip was found to be fully controlable and functional after irradiation with neutron fluence up to $8.18 \cdot 10^{15}$ n/cm^{-2}.

Further work on the study of radiation hardness of the test structures is planned, for example a measurement using ^{60}Co source. The results of this thesis will be taken into consideration in the development of new versions of the chip that will be designed.

Reactor core configuration
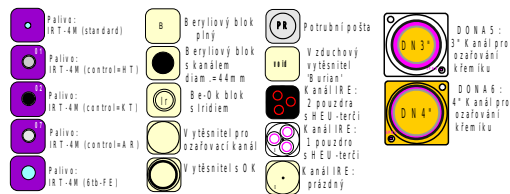
Konfigurace: K163 b.o.c
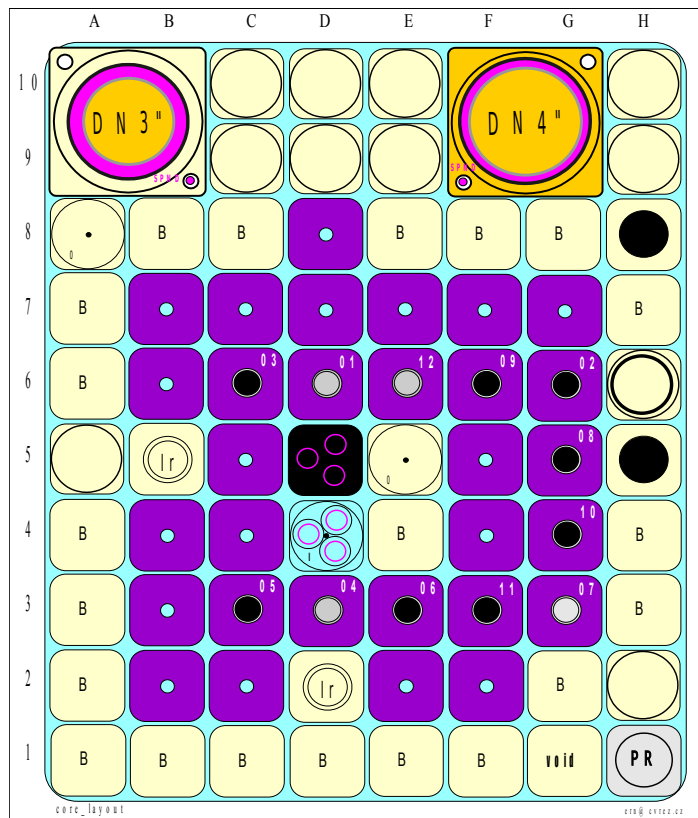
Figure A.1: The configuration of the reactor core during the irradiation of the samples. [44]

References

[1] G. F. Knoll, *Radiation detection and measurement; 4th ed.* New York, NY: Wiley, 2010.

[2] "Planck reveals an almost perfect Universe." `http://www.esa.int/Our_Activities/Space_Science/Planck/Planck_reveals_an_almost_perfect_Universe`, 2014. [Online; accessed 2-May-2014].

[3] K. Nakamura *et al.*, "Review of Particle Physics," *Journal of Physics G*, vol. 37, p. 075021, 2010.

[4] D. Griffiths, *Introduction to Electrodynamics.* Prentice Hall, 1999.

[5] J. Horejsi, *Fundamentals of Electroweak Theory.* Charles University Prague: The Karolinum Press, 2003.

[6] W. E. Nervik, "Spontaneous Fission Yields of Cf^{252}," *Physical Review*, vol. 119, pp. 1685–1690, Sept. 1960.

[7] "Wolfram Mathematica9 Reference Center." `http://reference.wolfram.com/mathematica/ref/LandauDistribution.html`, 2014. [Online; accessed 2-May-2014].

[8] "Wikipedia Commons." `http://commons.wikimedia.org/wiki/`, 2014. [Online; accessed 2-May-2014].

[9] J. H. Hubbell, H. A. Gimm, and I. Overbo, "Pair, triplet, and total atomic cross sections (and mass attenuation coefficients) for 1 Mev-100 Gev photons in elements Z=1 to 100," *Journal of Physical and Chemical Reference Data*, vol. 9, no. 4, pp. 1023–1148, 1980.

[10] ICRP 1990, "1990 Recommendations of the International Commission on Radiological Protection," ICRP Publication 60. Ann. ICRP, vol. 21, no. 1 - 3.

[11] ICRP 2007, "The 2007 Recommendations of the International Commission on Radiological Protection," ICRP Publication 103. Ann. ICRP, vol. 37, no. 2 - 4.

[12] A. Peisert, "Silicon microstrip detectors," in *Instrumentation in High Energy Physics*, ch. 1, pp. 1–79, 1992.

[13] G. Bertolini and A. Coche, *Semiconductor detectors.* Amsterdam : North-Holland, 1968.

[14] L. Rossi, *Pixel Detectors: From Fundamentals to Applications.* Particle Acceleration and Detection, Springer, 2006.

[15] G. Lutz, *Semiconductor Radiation Detectors: Device Physics.* Accelerator Physics Series, U.S. Government Printing Office, 1999.

[16] W. Brinkman, D. Haggan, and W. Troutman, "A history of the invention of the transistor and where it will lead us," *Solid-State Circuits, IEEE Journal of*, vol. 32, pp. 1858–1865, Dec 1997.

[17] H. Spieler, *Semiconductor Detector Systems*. Oxford scholarship online, OUP Oxford, 2005.

[18] "Encyclopaedia Britannica." `http://www.britannica.com/EBchecked/topic/544301/silicon-Si`, 2014. [Online; accessed 2-May-2014].

[19] M. Moll, "Radiation damage in silicon particle detectors – microscopic defects and macroscopic properties –," Master's thesis, Universität Hamburg, 1999.

[20] "OCI Company, South Korea." `http://www.oci.co.kr/eng/product/product_content.asp?code=E`, 2014. [Online; accessed 2-May-2014].

[21] S. M. Sze, *Semiconductor Devices: Physics and Technology; 3rd ed.* Wiley, 2012.

[22] J. Czochralski, "Ein neues Verfahren zur Messung der Kristallisationsgeschwindigkeit der Metalle," *Zeitschrift für Physikalische Chemie*, vol. 92, pp. 219–221, 1918.

[23] H. C. Theuerer, "Method of preparing silicon," Aug 25 1959. US Patent 2,901,325.

[24] G. Lindström *et al.*, "Developments for Radiation Hard Silicon Detectors by Defect Engineering: Results by the CERN RD48 (ROSE) Collaboration," *ROSE Collaboration*, 2000.

[25] The ATLAS collaboration, "Atlas experiment public pages." `http://atlas.ch`, 2014. [Online; accessed 2-May-2014].

[26] S. Gaalema, "Low noise random-access readout technique for large pin detector arrays," *Nuclear Science, IEEE Transactions on*, vol. 32, no. 1, pp. 417–418, 1985.

[27] E. H. Heijne, "Semiconductor micropattern pixel detectors: a review of the beginnings," *Nucl. Instrum. Methods Phys. Res., A*, vol. 465, no. 1, pp. 1 – 26, 2001.

[28] B. Gossick, "Disordered regions in semiconductors bombarded by fast neutrons," *Journal of Applied Physics*, vol. 30, no. 8, pp. 1214–1218, 1959.

[29] H. Spieler, "Introduction to radiation-resistant semiconductor devices and circuits," in *AIP Conference Proceedings*, vol. 390, p. 23, 1997.

[30] G. Lindstrom, "Radiation damage in silicon detectors," *Nucl.Instrum.Meth.*, vol. A512, pp. 30–43, 2003.

[31] ASTM E722-85 and ASTM E722-93 (revision 1993)

[32] M. Huhtinen, "Simulation of non-ionising energy loss and defect formation in silicon," *Nucl. Instrum. Methods Phys. Res., A*, vol. 491, no. 1–2, pp. 194 – 215, 2002.

[33] S. Messenger, E. Burke, G. Summers, and R. Walters, "Limits to the application of NIEL for damage correlation," *Nuclear Science, IEEE Transactions on*, vol. 51, no. 6, pp. 3201–3206, 2004.

[34] G. Lutz, "Effects of deep level defects in semiconductor detectors," *Nucl. Instrum. Methods Phys. Res., A*, vol. 377, no. 2–3, pp. 234 – 243, 1996.

[35] M. Moll, E. Fretwurst, and G. Lindström, "Leakage current of hadron irradiated silicon detectors: material dependence," *Nucl. Instrum. Methods Phys. Res., A*, vol. 426, no. 1, pp. 87–93, 1999.

[36] M. Moll, "Summary of the 3rd Rose status report," CERN-OPEN-2000-305, Mar 2000.

[37] G. Lindstrom, M. Moll, and E. Fretwurst, "Radiation hardness of silicon detectors: A challenge from high-energy physics," *Nucl.Instrum.Meth.*, vol. A426, pp. 1–15, 1999.

[38] R. Wunstorf, "Radiation hardness of silicon detectors: current status," *Nuclear Science, IEEE Transactions on*, vol. 44, pp. 806–814, Jun 1997.

[39] J. Schwank, M. Shaneyfelt, D. Fleetwood, J. Felix, P. Dodd, P. Paillet, and V. Ferlet-Cavrois, "Radiation effects in MOS oxides," *Nuclear Science, IEEE Transactions on*, vol. 55, no. 4, pp. 1833–1853, 2008.

[40] C. Kittel, *Introduction to solid state physics*. Wiley, 1968.

[41] "Atlas of neutron capture cross-sections." `https://www-nds.iaea.org/ngatlas2/`, 2014. [Online; accessed 2-May-2014].

[42] Pelowitz *et al.*, *MCNPX USER'S MANUAL Version 2.7.0 – LA-CP-11-00438*. Los Alamos National Laboratory, 2011.

[43] M. Chadwick *et al.*, "ENDF/B-VII.0: Next Generation Evaluated Nuclear Data Library for Nuclear Science and Technology," *Nuclear Data Sheets*, vol. 107, no. 12, pp. 2931 – 3060, 2006. Evaluated Nuclear Data File ENDF/B-VII.0.

[44] "Research reactor LVR-15." `http://www.cvrez.cz/en/infrastructure/research-reactor-lvr-15/`, 2014. [Online; accessed 2-May-2014].

[45] A. Ortiz-Conde, F. G. Sánchez, J. Liou, A. Cerdeira, M. Estrada, and Y. Yue, "A review of recent MOSFET threshold voltage extraction methods," *Microelectronics Reliability*, vol. 42, no. 4–5, pp. 583 – 596, 2002.

[46] D. Sharma, A. Chandorkar, and S. J. Vaidya, "Neutron induced oxide degradation in mosfet structures," in *Physical and Failure Analysis of Integrated Circuits, 2003. IPFA 2003. Proceedings of the 10th International Symposium on the*, pp. 151–155, July 2003.